

FUSE Observation of the Narrow Line Seyfert 1 Galaxy RE 1034+39: Dependence of Broad Emission Line Strengths on the Shape of the Photoionizing Spectrum¹

Darrin A. Casebeer, Karen M. Leighly, and E. Baron

*Department of Physics and Astronomy, The University of Oklahoma, 440 W. Brooks St.,
Norman, OK 73019*

casebeer@nhn.ou.edu

ABSTRACT

We present analysis from simultaneous *FUSE*, *ASCA*, and *EUVE* observations, as well as a reanalysis of archival *HST* spectra, from the extreme Narrow-line Seyfert 1 Galaxy RE 1034+39 (KUG 1031+398). RE 1034+39 has an unusually hard spectral energy distribution (SED) that peaks in the soft X-rays. Its emission lines are unusual in that they can all be modelled as a Lorentzian centered at the rest wavelength with only a small range in velocity widths. In order to investigate whether the unusual SED influences the emission line ratios and equivalent widths, we present three complementary types of photoionization analysis. The *FUSE* spectrum was particularly important because it includes the high-ionization line O VI. First, we use the photoionization code *Cloudy* and the SED developed from the coordinated observations to confirm that the emission lines are consistent with observed hard SED. The best model parameters were an ionization parameter $\log(U) \approx -2$ and a hydrogen number density $\log(n_H) = 9.75$ [cm⁻²]. Second, we present a Locally Optimally-emitting Cloud model. This model produced enhanced O VI as observed, but also yielded far too strong Mg II. Third, we develop a series of semi-empirical SEDs, run *Cloudy* models, and compare the results with the measured values using a figure of merit (FOM). The FOM minimum indicates similar SED and gas properties as were inferred from the one-zone model using the RE 1034+39 continuum. Furthermore, the FOM increases sharply toward softer continua, indicating that a hard SED is required by the data in the context of a one-zone model.

Subject headings: line: formation — quasars: emission lines — quasars: individual (KUG 1031+398)

1. Introduction

The broad emission lines in Active Galactic Nuclei (AGN) are powered primarily by photoionization (e.g., Osterbrock 1989). There is copious evidence leading to this conclusion. For example, the emission lines are observed to vary in response to variations in the continuum. Also, the flux in strong lines is correlated with the continuum flux. Knowing that photoionization powers the emission lines, we can easily predict which lines will be strong. Photoionization removes electrons from hydrogen atoms; therefore, recombination products such as Ly α should be strong. The free electrons collide with ions from other elements, exciting those from abundant elements that are isoelectronic with lithium, such as C³⁺, because the excitation potential of their first excited states is low. Many of these excited states are short-lived; the ion returns to ground state with emission of a photon which then escapes the gas, cooling it. Thus, we expect lines such as C IV λ 1549 to be strong as well.

For this cooling channel to be effective, three-times ionized carbon atoms must be present in the gas. Therefore, the line emission should be governed by the photoionization parameter $U = \Phi / nc$ where Φ is the photoionizing flux, generally in units of photons $\text{cm}^{-2} \text{s}^{-1}$, and n is the gas density in units of cm^{-3} . The ionization parameter is the ratio between the photon density, which drives photoionization, and the gas density, which controls recombination. Thus, since C IV being strong implies the presence of C³⁺ in the gas, it also implies a particular value or range of values for the ionization parameter (more specifically, the ratios of Ly α to C IV and of C IV to C III). A typical value of the ionization parameter inferred is around $\log(U) = -1.5$ (e.g., Kwan & Krolik 1981).

But does the presence of C IV really imply a particular ionization parameter? Perhaps it really is telling us that gas with a range of ionization parameters, corresponding to a range of photon fluxes and densities, is present, but gas with the ionization parameter suitable for C IV production happens to emit most efficiently, due to the easy excitation of the C³⁺ ion. This would cause the integrated line emission to be weighted toward gas with copious C³⁺ present, but would not preclude the presence of less effectively-emitting gas. These ideas were proposed by Baldwin et al. (1995) as the Locally Optimally-emitting Cloud model.

This simple conceptual picture of photoionization in AGN provides a zeroth-order understanding of why the line emission is similar in all objects, and why the same strong lines are usually seen. However, there are some significant trends in the emission line properties that cannot be explained directly using this zeroth-order understanding. Furthermore, there

¹Based on observations made with the NASA-CNES-CSA Far Ultraviolet Spectroscopic Explorer. FUSE is operated for NASA by the Johns Hopkins University under NASA contract NAS5-32985.

are numerous examples of objects or classes of objects whose emission lines differ from that of the average quasar. These trends and the presence of classes of unusual objects require more sophisticated models than the zeroth-order picture presented above. This is a good thing; there are many fundamental things we don't know about the broad-line region even after years of study, including the geometry, the dynamics of the gas, and the origin of the gas. With such a large number of potentially variable parameters, our task may seem hopeless. That is far from the case, and in fact, the potential for solving this problem is orders of magnitude higher than it was when the first models were being developed due to the availability of powerful computers, increasingly-sophisticated models, and large samples of high-quality spectra from, e.g., the Sloan Digital Sky Survey.

One of the factors that may affect the emission lines in AGN is the shape of the spectral energy distribution (SED). AGN are known to have broad spectral energy distributions, with almost equal power emitted per logarithmic frequency range between the infrared and X-ray bands (e.g., Peterson 1997). Their emission lines are powered largely by the bandpass from ~ 4 eV through the soft X-rays, although the regions of the spectrum outside this range can contribute through heating. This part of the spectral energy distribution is thought to be primarily the emission of the accretion disk, with the higher energies above ~ 1 keV or so emitted by a Comptonizing corona. Theoretically, the continuum emitted by the accretion disk should depend on the mass and accretion rate (e.g., Frank, King, & Raine 2002; Ross, Fabian, & Mineshige 1993), the accretion disk geometry (e.g., Zdziarski & Gierlinski 2004), and inclination (e.g., Laor & Netzer 1989; Puchnarewicz et al. 2001). In the simplest thin disk models, accretion onto smaller black holes, and accretion at a higher rate relative to the Eddington value predicts hotter disks (e.g., Shakura & Sunyaev 1973), and correspondingly overall harder spectral energy distributions. The X-ray emission arising from Comptonization by a hot optically-thin component may also be affected by the accretion rate as the power for the hot component must ultimately come from accretion. In some models, all of the accretion energy is deposited initially into the corona and then a fraction is reprocessed by the disk (Svensson & Zdziarski 1994). Other models propose an accretion/evaporation scenario in which the disk and corona are coupled (Różanska & Czerny 2000a,b). In these models, the amount of emission from the corona relative to that from the disk depends on the accretion rate relative to the Eddington value, with the coronal emission becoming less important at high accretion rates (e.g., Bechtold et al. 2003). In addition, at very low accretion rates, the accretion should have a different geometry (e.g., Ho 2003); a hot, optically-thin thermal plasma may dominate the inner region, producing a much different spectral energy distribution that lacks a big blue bump.

Thus, there is a clear theoretical expectation that the spectral energy distributions in AGN should take on a range of shapes. What is the observational evidence that such a

range exists? First, it is worth noting that there are difficulties in measuring the intrinsic spectral energy distribution. Since AGN vary at all wavelengths, observations in different wavebands should in principle be at least contemporaneous. Absorption and reddening in the host galaxy or in the AGN itself poses another serious complication. Finally, because of absorption, the portion of the observed-frame spectrum between 13.6 and ~ 100 eV cannot be observed at all.

Nevertheless, there is some solid evidence AGN are not characterized by a single spectral energy distribution; a range in shapes exists. For example, studies of samples of objects shows a range of SEDs (e.g., Elvis et al. 1994). In addition, α_{ox} , the point-to-point slope between 2500Å and 2 keV, has been repeatedly observed to depend on the UV luminosity (Wilkes et al. 1994; Bechtold et al. 2003; Vignali et al. 2003). Among objects in a sample of soft X-ray selected AGNs, a correlation between the optical/UV continuum slope and the X-ray photon index has been found, such that objects with bluer optical continua have steeper X-ray spectra (Grupe et al. 1998). Also, a *FUSE* composite spectrum is observed to be harder than an *HST* composite over the same rest bandpass; as the *FUSE* spectra are from relatively lower luminosity objects, this result is attributed to luminosity-dependent evolution of the spectral energy distribution (Scott et al. 2004).

Indirect evidence for a range of spectral energy distributions among AGNs is provided by the observation that the ratio of optical depth of He II Ly α to that H I Ly α in the era of He II reionization fluctuates on small redshift scales. This is inferred to be caused by the response of these ions to a range in continuum shapes due to the difference in ionization potentials (Shull et al. 2004.) However, at least part of this range in continua may certainly be caused by reddening/absorption.

Emission lines in AGNs, while broadly similar, clearly show trends and dependencies that are plausibly dependent on the spectral energy distribution. The first trend discovered was the Baldwin effect, which is the empirical inverse relationship of emission line (e.g., C IV) equivalent width with luminosity (Baldwin 1977; for a review, Osmer & Shields 1999). Initially, several models were proposed for this effect. For example, Mushotzky & Ferland (1984) posited a luminosity-dependent ionization parameter; a luminosity-dependent covering fraction was also thought to be possibly important. More recently, observational evidence has been repeatedly found that the slope of the Baldwin effect is steeper for high-ionization lines than for low-ionization lines (Osmer, Porter, & Green 1994; Green 1996; Espey & Andreadis 1999; Wilkes et al. 1999; Green, Forster, & Kuraszkiewicz 2001; Dietrich et al. 2002; Shang et al. 2003; Warner et al. 2004). This is interpreted appealingly as evidence that, as the luminosity increases, the spectral energy distribution softens, resulting in a more rapid decrease in the highest ionization lines. Further evidence supporting this

view comes from observed correlations between continuum shape indicators such as α_{ox} and line equivalent width (Zheng, Kriss & Davidsen 1995; Wang et al. 1998; Green 1998; Wilkes et al. 1999; Scott et al. 2004). Thus, it appears that the Baldwin effect is a phenomenon that depends principally on the shape of the spectral energy distribution, and its corresponding dependence on luminosity.

Interestingly, it has been found that Narrow-line Seyfert 1 galaxies show a Baldwin effect that is offset from that shown by other Seyferts and quasars (Wilkes et al. 1999; Leighly & Moore 2004; Leighly et al. in prep.). This might be related to the fact that the cores of the lines show a stronger Baldwin effect than the wings of the lines (Osmer, Porter & Green 1994; Shang et al. 2003; Warner et al. 2004). It is possibly an indication of a different BLR geometry for this class of objects (e.g., Leighly 2004).

Theoretical confirmation of this model for the Baldwin effect is promising but not yet completely firm. Korista, Baldwin & Ferland (1998) use an LOC model and find that the slope dependence of the data is consistent with an evolving spectral energy distribution. On the other hand, Korista, Ferland & Baldwin (1997) show that there may be difficulties explaining the strength of the He II line using continua developed from composite spectra.

The second important trend for line emission in AGN is the Eigenvector 1 dependence. Boroson & Green (1992), in a principle components study of spectra from PG quasars, discovered that much of the variance among optical emission lines is correlated such that narrow lines are associated with strong Fe II and weak [O III] emission. Later work shows a relationship with the steepness of the X-ray spectrum (e.g., Brandt & Boller 1999), and an extension to the UV spectra (e.g., Wills et al. 1999). The physical driver for Eigenvector 1 is thought to be the accretion rate relative to Eddington (e.g., Leighly & Moore 2004 and references in the introduction). Precisely how this works has not been yet clearly delineated, but it could be mediated by the spectral energy distribution. For example, Wandel & Boller (1998) propose that the steeper soft X-ray spectrum seen in NLS1s translates to a more powerful extreme UV excess that would cause the emission lines to originate from a larger radius where velocities are smaller. Kuraszkiewicz et al. (1999) attribute the characteristic UV emission-line ratios to higher densities in the broad-line region. They examine a two-phase BLR model, and suggest that the higher densities arise naturally in this model due to the hotter big blue bumps. Wills et al. (1999) infer high densities in the BLR as well, from the Si III]/C III] ratio. However, as shown in §7.3, this ratio can depend on the spectral energy distribution, because in some regions of the U–SED-shape parameter space, Si III] will dominate the cooling.

The spectral energy distribution can influence the line properties in another way. Leighly & Moore (2004) and Leighly (2004) show that in a sample of Narrow-line Seyfert 1 galaxies,

the degree of blueshift of C IV is correlated with α_{ox} , such that objects that are relatively weak in X-rays have more highly blueshifted lines. This makes perfect sense in the context of radiative-line driven wind models (e.g., Proga, Stone & Kallman 2000), because the way that the UV and X-rays play competing roles in the formation of such winds. Specifically, the UV accelerates the wind, while the X-rays tend to impede the wind because they can overionize it, destroying the ions that scatter the UV emission. So, even though objects with relatively strong X-rays can have winds, due to self-shielding, or preabsorption of soft X-rays before reaching the wind gas (Murray et al. 1995; Proga & Kallman 2004), objects with relatively strong UV emission and weak X-ray emission will always drive faster, more massive winds.

Leighly (2004) also notes that the spectral energy distribution can influence the strengths of the emission lines indirectly via the wind. It has long been suspected that low- and intermediate-ionization lines are produced in a different region than high-ionization lines. The evidence for this comes from modeling of the line emission (e.g., Collin-Souffrin et al. 1982, 1986; Wills, Netzer, & Wills 1985), and from the difference in profiles (e.g., Collin-Souffrin et al. 1988; Baldwin 1997). One of the puzzling features in quasar spectra is the observed trend for objects with strong high-ionization line emission such as N V to have strong low-ionization line emission such as Si II (Wills et al. 1999). Leighly (2004) show that low-ionization line emission can be enhanced if the continuum illuminating that emission region is first filtered through the wind. Such a continuum is deficient in helium-continuum photons, as they are all absorbed by the wind, and thus can only excite relatively low-ionization species.

We are currently investigating the effects of the spectral energy distribution on the broad-line emission and kinematics in AGN. In this installment, we present an analysis of spectra from a Narrow-line Seyfert 1 galaxy RE 1034+39 ($z = 0.043$). This object is well known for its unusual spectral energy distribution. Puchnarewicz et al. (1995), Puchnarewicz, Mason, & Siemiginowska (1998), and Puchnarewicz et al. (2001) have reported optical, UV and X-ray observations of this object. While the optical and UV spectra of the typical AGN rises toward the blue, forming the big blue bump, RE 1034+39's optical/UV spectrum is rather red. The big blue bump appears instead in the X-ray spectrum: it appears to peak at ~ 100 keV, and the high energy turnover toward long wavelengths appears to be in the soft X-rays (Puchnarewicz et al. 1995). This unusual spectral energy distribution was confirmed by the *BeppoSAX* observation conducted in 1997 and reported by Puchnarewicz et al. (2001). The unusual spectral energy distribution has been modelled as an edge-on accretion disk (Puchnarewicz et al. 2001) and as an irradiated accretion disk (Soria & Puchnarewicz 2002).

Given RE 1034+39's hard spectral energy distribution, one might expect that there

would be strong high-ionization line emission in its UV spectrum, assuming that the line emitting gas sees the same continuum that we do. To test this hypothesis, we obtained a *FUSE* observation of RE 1034+39, along with coordinated *EUVE* and *ASCA* X-ray observations. We present the analysis of these spectra here, as well as a reanalysis of the archival *HST* spectrum (§2). In the next three sections, we present three complementary types of photoionization analysis. First, using the spectral energy distribution constructed from the coordinated observations, we ran *Cloudy* (Ferland 2001) photoionization models to determine the conditions of the line emitting region, and ascertain whether the line equivalent widths and ratios are consistent with the extreme spectral energy distribution for a single-zone model (§3). We then look at how well the lines could be modeled in the LOC scenario (§4). Third, we consider a range of semi-empirical spectral energy distributions presented in the Appendix, and compare the predicted line emission as a function of SED (and other parameters) with that of RE 1034+39 (§5). We discuss the results in §6, and present auxiliary material in an Appendix, §7.

2. Multiwavelength Observations and Data Analysis

2.1. *FUSE* Observation

The *Far Ultraviolet Spectroscopic Explorer (FUSE)*² was launched 1999 June 24. *FUSE* provides unprecedented sensitivity and resolution over the 905–1187Å bandpass, which contains rest wavelength transitions from many important atoms and molecules (Moos et al. 2000; Sahnou et al. 2000). The *FUSE* observation of RE 1034+39, coordinated with observations using *ASCA* and *EUVE*, was approved as part of the Cycle 1 Guest Investigator observing program.

The observing log for the *FUSE* observation is given in Table 1. The raw *FUSE* data were downloaded and reprocessed. At the time that the analysis was done, CALFUSE v2.0 had not yet been released, and the Beta version was not fully functional; therefore, we used CALFUSE v1.8.7 with some enhancements from v2.0 as described below. We recently re-ran the pipeline using CALFUSE v2.4 and confirmed that the resulting spectra are indistinguishable from the ones that are presented here. RE 1034+39 is a faint object for *FUSE*; therefore, we used only the data obtained during the time that *FUSE* spent in the earth’s shadow. To reduce the background, we only used data within PHA channels 4–16 (e.g., Brotherton et al. 2002). This choice approximately halved the value of the constant

²<http://fuse.pha.jhu.edu/>

background component, but decreased the source flux by only $\sim 5\%$.

CALFUSE v1.8.7 approximated the background using a uniform image; however, the real detector background has considerable structure. In CALFUSE v2.0 and subsequent versions, this is accounted for by using real images of the background. In order to utilize this improvement in CALFUSE v1.8.7, we extracted the night-time background image from the v2.0 calibration files and used it instead of the v1.8.7 background image. We then ran the pipeline again. We adjusted the scaling and offset of the background image to the background level of the observation. To do this, we extracted spectra from two source-free regions of the detector in the observed image and the background image. A linear regression between the background and source vectors produced the scale and offset necessary to match the background file to the data. The background was suitably scaled and offset, and the pipeline script modified to use this background image.

We examined the two-dimensional images after background subtraction. The spectral trace was clearly visible for all telescope systems except SiC2. We take this as evidence that the image of the galaxy was not in the the slit for this telescope system, and we do not consider it further. The background subtraction appeared to be successful for most of the telescope/detector segments; however, we were unable to obtain a satisfactory background subtraction for the LiF2b spectrum, and we do not consider it further. The SiC1a spectrum was not used in the composite spectrum, due to low signal-to-noise ratio compared to the LiF1a spectrum which samples the same wavelength interval.

We examined the flux calibration between overlapping detector segments. The most noticeable difference was between LiF2a and LiF1b segments longward of 1140 Å. We expect that this difference may be due to the “worm” or shadowing of the detector by the grid wires above it in LiF1b. Therefore, we exclude data longward of 1140 Å for that segment, and average the two segments over the remainder of the overlapping interval.

Wavelength calibration V10 was used. The remaining spectra (LiF1a, combined LiF1b and LiF2a, SiC1b) were rebinned using an algorithm similar to the IRAF `trebin` script. The spectra were then concatenated, and the result is shown in Fig. 1, after having corrected for the redshift ($z = 0.043$), and Galactic reddening $E(B - V) = 0.015$ mag, estimated from the infrared cirrus (Schlegel, Finkbeiner & Davis 1998), using the Cardelli, Clayton & Mathis (1989) reddening curve.

Uncertainties in spectra are rarely shown for *FUSE* spectra of AGN (e.g., Shang et al. 2005; Romano et al. 2002). This is possibly because the error column in the pipeline spectra aren’t very useful; the spectra contain only several photons per bin at full wavelength resolution. However, uncertainties on the spectra are useful to have for faint objects such as

AGN, so we developed a method to evaluate them. First, we ran the pipeline, outputting the intermediate products which include the “total” image (*_img.fit*) and the scaled background image (*_bkgd.fit*). The spectra at full wavelength resolution were extracted from these images using the nominal extraction regions (calibration files *spex1a009.fit*, etc) and collapsing in the y direction. The wavelength scale was obtained from the pipeline output spectrum. The total counts spectrum and background counts spectrum were rebinned to the desired bin size (in this case, 0.5Å) by summing the counts within each bin. Then the error counts spectrum was obtained by propagation of errors assuming Poisson statistics in each bin of the rebinned total and background spectra. The error spectrum was then “fluxed” using the appropriate calibration flux file (calibration files *flux1a008.fit*, etc.). The error spectrum is shown by the thick line in Fig. 1. This shows that no continuum flux was detected below $\sim 960\text{\AA}$ where only the SiC1b spectrum is available.

The shorter wavelength component of the O VI $\lambda 1034$ doublet (1031.93Å) is clearly detected, but the longer wavelength component (1037.62Å) is absent (Fig. 1). We suspect that the longer wavelength component does not appear because of residual background subtraction problems. Fig. 2 shows a section of the 2D LIF1 image after screening and before background subtraction. The spectral trace is clearly seen, and an enhancement corresponding to the 1037Å component is apparent. Fig. 2 also shows that the background is higher near the edge of the detector; the effective area is lower as well. Thus it proved to be impossible to tease the longer wavelength component of O VI from the noise. We note that there is an enhancement in the low signal-to-noise ratio Sic1a spectrum at 1037Å (shown as an inset in Fig. 1). Therefore, we base our analysis on the 1032Å component.

C III $\lambda 977$ was also detected, as well as $\text{Ly}\beta$ (see Section 2.6); however, N III and He II, low equivalent width lines sometimes seen in other FUV spectra from AGN (e.g., Brotherton et al. 2002; Hamann et al. 1998) are were not detected.

2.2. ASCA Observation

An *ASCA* observation was conducted simultaneously with the *FUSE* observation (Table 1). A standard configuration was used during the observation. The GISs were operated in PH mode throughout the observation. The SISs were operated in 1 CCD Faint and Bright mode at high and medium bit rate, respectively. The SIS energy gain was reprocessed using the latest calibration file (*sisph2pi_290301.fits*).

We used the same criteria as the rev 2 standard processing for our data selection³, except for the `ANG_DIST` (angular distance from the nominal pointing) criterion. The pointing accuracy was poor during this observation; therefore, we used a looser angular distance selection criterion. The sensitivity change due to the pointing error of 1.0 arcmin is about 10%; this is accounted for in the spectral fitting by the ancillary response file.

The source was detected at R.A. = $10^{\text{h}}34^{\text{m}}36^{\text{s}}$ and Decl. = $39^{\circ}38'56''$ (equinox 2000.0) in good agreement with the optical position within the *ASCA* position accuracy of $\sim 1'$. We accumulated the source photons from the circular regions centered on the source with radii of 4.0, 3.5 and 6.0 arcmin for the SIS-0, SIS-1 and GISs, respectively. The background data were accumulated from source-free regions on the detector. The average count rates from the source regions are 0.096 c s^{-1} and 0.059 c s^{-1} , and the background fractions are estimated to be $\sim 13\%$ and $\sim 33\%$ for each SIS and GIS, respectively.

We fitted each of the four spectra separately with a model consisting of a power-law with Galactic absorption ($N_H = 1.43 \times 10^{20} \text{ cm}^{-2}$; Murphy et al. 1996) in the whole energy band. The statistics were rather poor in this short observation; thus, this model is not rejected at 90% confidence level for any of the spectra. Then, we added a blackbody to the model to represent the soft excess component commonly seen in NLS1 spectra, and previously seen in this object (Pounds, Done & Osborne 1996; Leighly 1999). The fits were acceptable for all four spectra and χ^2 values were improved significantly (F-test confidence levels of 99 and 97% for SISs and GISs, respectively). All parameters are consistent among the four detectors. We also confirmed that the results from the faint and bright mode are consistent with those only from the faint mode data (which have better energy resolution). Finally we fit the SISs and GISs data simultaneously with a model of a power-law plus a black body attenuated by Galactic absorption. The best-fit parameters are summarized in Table 2.

The divergence of the SIS spectra at low energies has been reported, especially for observations performed near the end of the mission. An empirical correction for this has been proposed by Yaqoob et al. (2000)⁴. We applied this correction by introducing a fixed neutral absorption $N_H = 7.3 \times 10^{20} \text{ cm}^{-2}$, appropriate for the date of this observation, and discarding the SIS-1 data below 1 keV. The best-fit parameters from this fit are also listed in Table 3.

³http://adfwww.gsfc.nasa.gov/asca/processing_doc/proc/rev2/la_test/screen.html

⁴<http://heasarc.gsfc.nasa.gov/docs/asca/calibration/nhparam.html>

2.3. EUVE Observation

An EUVE observation was conducted simultaneously with the *ASCA* and *FUSE* observations (Table 1). A description of the standard reduction for the *EUVE* Deep Survey Instrument is given in Halpern, Leighly & Marshall (2003). RE 1034+39 is a reasonably bright target for *EUVE*. However, the observation was conducted during Solar Maximum, which strongly enhanced the background and resulted in noisy data. While the resulting light curve was formally significantly variable (χ_R^2 for a constant hypothesis was 1.99 for 53 degrees of freedom), we believe that the origin of the variability may be less-than-perfect background subtraction. We note that the average count rate observed ($0.036 \text{ count s}^{-1}$) during the coordinated observation is consistent with the rate observed ($0.037 \text{ count s}^{-1}$) during a quieter period three years earlier and is therefore consistent with the general lack of variability in this object (Puchnarewicz et al. 2001).

We use PIMMS (Portable, Interactive Multi-Mission Simulator; Mukai 1993) to estimate the flux. We assume that the spectrum is a power law with Galactic absorption of $N_H = 1.43 \times 10^{20} \text{ cm}^{-2}$. For a range of photon indices between 2.5–4.5, we predict an intrinsic flux at 0.15 keV observed frame of between 0.75–0.83 photons $\text{cm}^{-2} \text{ s}^{-1} \text{ keV}^{-1}$.

2.4. Archival HST FOS spectra

Our proposal for coordinated *HST* observations was not successful, so we analyzed the archival data from this object, previously presented by Puchnarewicz et al. (1998). We applied the most up-to-date calibration to the archival data. We used the Galactic absorption lines to check the wavelength calibration of the spectra and shifted them appropriately.

The *HST* data were obtained more than three years before the *FUSE* observations. Thus, variability between the observations was a concern; are we justified in using these archival data? We believe that we are, for two reasons. First, the *FUSE* and *HST* continua are separated by a gap of less than 20 Å, and the *FUSE* continuum appears to be consistent with an extrapolation of the *HST* continuum. Second, RE 1034+39 is well known for its general lack of variability (Puchnarewicz et al. 2001).

2.5. Analysis of the Emission Lines

In this section, we describe our extraction of the emission-line parameters from the spectra, and discuss some features of the results. The spectra were fitted using the *Specfit*

module in IRAF (Kriss 1994). The results are given in Table 3 and Fig. 3.

Puchnarewicz et al. (1998) found no evidence for intrinsic absorption lines in the *HST* spectra; our reanalysis did not uncover any either. The high resolution and good sensitivity obtained in the *FUSE* spectrum revealed a number of weak absorption features on O VI (Fig. 4). The wavelengths of all of these features were consistent with Galactic molecular hydrogen absorption. Thus, we find no evidence for intrinsic O VI absorption in RE 1034+39.

Preliminary examination showed that the spectra consisted of a smooth continuum and narrow lines that are generally not strongly blended. Also, RE 1034+39 lacks the strong Fe II multiplets frequently found in Narrow Line Seyfert 1 galaxies that can interfere with spectral fitting. Therefore, we modeled the continuum locally using a linear function around each line or blend. The line profile of the permitted and semi-forbidden lines could be modeled well with a Lorentzian profile and there appeared to be little evidence for a difference in shape between the high and low-ionization lines such as has been observed in some Narrow Line Seyfert 1 galaxies (e.g., Leighly & Moore 2004a). In fact, we found that we could obtain an acceptable fit if the wavelength of each line were fixed to the laboratory wavelength, allowing only the width and flux to vary. Widths of doublets and multiplets were constrained to be equal. Doublet and multiplet intensities of some lines were constrained as follows. The relative line intensities for O IV λ 1402 multiplet were constrained using the treatment described by Nussbaumer & Storey (1982). Lines emitted from the same upper levels depend only on relative transition probabilities; this is the case for the λ 1399.77 and λ 1407.39 lines where a ratio of 1 was calculated, the λ 1397.20 and λ 1404.81 lines where a ratio of 0.13 was calculated. The density dependent components of O IV λ 1402 were taken from Nussbaumer & Storey (1982). The emission line features are consistent with a density of $n_H = 10^{10} \text{ cm}^{-3}$ given a temperature of the gas of $1.5 \times 10^5 K$. We point out however that this feature is very weak and blended, and we cannot use it to constrain the density of the emitting gas.

Fig. 3 demonstrates that our assumption that the line profile is uniformly Lorentzian is well justified, in most cases. There are a few discrepancies. As discussed in Section 2.1, the O VI line is near the edge of the Lif1a detector, so that the only the 1032Å component is measured. We also found that the blue component is weaker than the red component of the Mg II doublet. This is not expected physically, because the statistical weight of the blue component is twice that of the red component. We investigated the possibility that the profile was affected by bad diodes or Galactic absorption lines, but were unable to find the reason for this discrepancy. Also, we found that the He II λ 1640 line displays a blue wing; this was also reported by Puchnarewicz et al. (1998). This is the only line in the spectrum that displays such a feature. It is possible that it originates in recombination in optically

thin, highly ionized gas.

In Fig. 5, we plot the velocity width of the brighter ($F_\lambda > 1.5 \times 10^{-14}$ erg cm $^{-2}$ s $^{-1}$ for the multiplet), and least-blended emission lines as a function of their ionization potential (O VI, Ly α , N V, C IV, Si III], C III], Mg II). We find that most of the higher-ionization lines have slightly larger velocity widths than lower-ionization lines. Such trends have been seen before (e.g., Baldwin 1997), and they are consistent with our understanding based on reverberation mapping results (e.g., Peterson 1998) that the broad-line region is typically radially stratified. The exception is He II. This line is different than the other high-ionization lines in that it has a blue wing; it is possible that deblending the blue wing artificially narrowed the line core. RE 1034+39 is unusual in that the line profiles have the same shape and are all centered at their rest wavelength; in other objects, high ionization lines are not only broader but sometimes strongly blueshifted (e.g., Leighly & Moore 2004a). RE 1034+39 is also unusual in that the range of velocity widths of lines of different ionization is small.

The measured equivalent width of the 1031.9Å component of the O VI line is 29Å. As noted in §2.1, we could not measure the 1037.6 Å component because of high background. If we assume that the gas is very optically thick, these two emission lines will have the same equivalent width, and the equivalent width of the doublet would be 58Å. Alternatively, in the optically thin regime, the 1037.6 Å component should have half the flux of the 1031.9Å component, and the total equivalent width would be 43Å. In either case, given the low luminosity of $\log L_{2500} = 28.3$ [ergs s $^{-1}$], we find that it is roughly consistent with the O VI Baldwin effect presented by Kriss (2001).

In Table 4, we present a comparison of the bright emission line fluxes with that of Ly α for RE 1034+39 and the same quantities obtained from three composite spectra: the LBQS composite (Francis et al. 1991), the radio-quiet composite from *HST* spectra (Zheng et al. 1997), and a composite spectrum from the FIRST Bright Quasar Survey (Brotherton et al. 2001). We find that the biggest difference is in the measurement of O VI: the value from RE 1034+39 is much larger with respect to Ly α than from any of the other composites. It should be noted, however, that the LBQS and FIRST composites are made with observed-frame optical spectra, where Ly α forest absorption could reduce the flux of O VI. However, this does not explain the difference with respect to the *HST* composite. RE 1034+39 also has stronger He II and weaker Mg II than the composites.

2.6. The Spectral Energy Distribution of RE 1034+39

The spectral energy distribution (SED) of RE 1034+39 constructed from the *HST*, *FUSE*, *EUVE* and *ASCA* data is shown in Fig. 6. For comparison, we show the *Cloudy* AGN continuum. The strong soft excess peaking in the EUV first reported by Puchnarewicz et al. (1995) is clearly seen.

The shape of the SED is frequently roughly parameterized by α_{ox} , the point-to-point power law slope between 2500 Å and ~ 2 keV. We infer $\alpha_{ox} = 1.22$ for RE 1034+39. Wilkes et al. (1995) find that this parameter is correlated with the log of the luminosity at 2500 Å. For an object with $\log_{10}(l_{opt}) = 28.3$ (for $H_0 = 50$, $\Lambda_0 = 0$), their regression predicts $\alpha_{ox} = 1.29$. It should be noted that there are only 5 objects with lower optical luminosity than RE 1034+39 in the Wilkes et al. sample; these objects cluster around $\log L_{2500} \approx 28$, and their α_{ox} 's are ~ 1.6 . This suggests that RE 1034+39 has a markedly flat α_{ox} compared with other AGN of its luminosity.

Puchnarewicz et al. (1995) reported that the optical/UV continuum could be described by a power law ⁵ with index $\alpha_{opt} \sim 0.9$. This is somewhat steeper than that of the typical quasar (0.33 with rms dispersion of 0.59; Natali et al. 1998). Our reanalysis of the *HST* spectra, in combination with the *FUSE* spectrum, shows that the spectrum subtly steepens at short wavelengths, and is consistent with a flatter slope of $\alpha_{opt} = 0$ shortward of 2200 Å up to O VI. The subtle upturn is seen in the inset in Fig. 6. Shortward of O VI the slope appears to become flatter in the *FUSE* spectrum. We have no explanation for this; it is possible that the object is not in the slit for all detectors at all times, creating a flux misalignment between the separate segments of the spectrum. Because the continuum is not detected in the SiC1a detector (Fig. 1), we cannot use that spectrum to check and repair the flux alignment (e.g., Brotherton et al. 2001). Regardless, we observe, as did Puchnarewicz et al. 1995, that the optical/UV spectrum does not extrapolate to the flux in the soft X-rays.

3. One-zone Photoionization Models using the RE 1034+39 Continuum

A primary goal of this paper is to see whether RE 1034+39's emission line equivalent widths and ratios are consistent with its unusual spectral energy distribution. To do this, we perform photoionization modeling using the photoionization code *Cloudy* (Version 94.00; Ferland 2001). In this section, we first attempt to model the lines with a one-zone model, making the simplifying assumption that the gas emitting the lines is described by a

⁵ α_{opt} defined by $F_\nu \propto \nu^{-\alpha_{opt}}$

single photon flux and density. This assumption is partially justified by the similar profile and velocity width of the emission lines (§2). In §4, we relax this assumption, and compute a Locally-Optimally emitting cloud model for RE 1034+39.

Cloudy requires as input the spectral energy distribution, the photon flux, the hydrogen number density, and the column density of the gas. To compute the line equivalent widths, a covering fraction is required. Gas metallicity can also be specified; we found reasonably good results with solar metallicity, so we did not vary this parameter.

To obtain the spectral energy distribution, we used the observations shown in Fig. 6. The region between the *FUSE* spectrum, which extends to 960Å in the rest frame, and the *EUVE* point at 0.156 keV is not observable, and we simply extrapolate using a power law over this region. Outside of the observed band pass, we used the *Cloudy* AGN SED. Specifically, we assumed that the spectrum continues toward longer wavelengths to 10 microns before dropping sharply toward the radio. Also, as there is no spectral information above 10 keV for this object, we extrapolate the hard X-ray power law to 100 keV before requiring it to drop off sharply toward higher energies. Compared with the *Cloudy* AGN continuum, that of RE 1034+39 begins to increase toward the UV at shorter wavelengths, and is much stronger in the soft X-rays.

The photon flux, Φ , expressed in photons $\text{cm}^{-2} \text{s}^{-1}$, and the hydrogen number density, n_H , expressed in cm^{-3} , were the parameters that we sought to constrain with the simulations. To do so, we computed grids of models over a range of Φ ($16.0 < \log(\Phi) < 20.75$; $\Delta \log(\Phi) = 0.125$) and n_H ($8.5 < \log(n_H) < 11.5$; $\Delta \log(n_H) = 0.125$). Thus, we examined gas conditions over a large range of ionization parameter ($-4.0 < \log(U) < -0.5$).

For the column density, we use the parameter $\log(N_H^{max})$, which is defined as $\log(N_H) - \log(U)$, where N_H is the column density (see also Leighly 2004). This parameter is a convenient one for studies of photoionized gas because it adjusts the column density to account for the ionization parameter. Therefore, for a particular value of N_H^{max} , we probe to the same depth in terms of hydrogen ionization fraction regardless of the ionization parameter. Initially, we tried a model that is optically thin to the hydrogen continuum, in which $\log(N_H^{max})$ was set equal to 21.5. This model was not able to produce the line equivalent widths and ratios; this is not surprising, because observed low-ionization lines such as Mg II are produced near the hydrogen ionization front. Ultimately, we used $\log N_H^{max} = 26$ because the slab is then sufficiently thick to produce observed low-ionization lines such as C II. Emission line fluxes and ratios for models that are optically thin to the hydrogen continuum can be very sensitive to the column density (e.g., Leighly 2004); optically-thick models are much less sensitive, and therefore we fix this parameter.

The similar line profiles for the high-, intermediate-, and low-ionization lines in this object suggest that all the lines are produced in gas with similar or uniform properties. Even though this may not be a precisely accurate physical description of the emission line region, as a first step, we investigate whether one region of the $\Phi - n_H$ parameter space can produce all the lines. To do this, we plot the contours for which the model equivalent widths equal the measured equivalent widths for all of the most prominent emission lines (e.g., Baldwin et al. 1996). The equivalent width of a line depends on the gas covering fraction. We varied this parameter, and determined that we could obtain a solution in which the most contours overlapped in the smallest region for a covering fraction of 0.1. The results are shown in Fig. 7 for the high-ionization lines (O VI, N V, C IV, and He II), and for the intermediate- and low-ionization lines (C III λ 977, C II λ 1335, O III] λ 1666, Si III], C III], and Mg II). Ly α was not plotted. We found that the predicted value of Ly α equivalent width was ~ 1.9 – 3.1 times higher than the observed value in the box-enclosed region. This may indicate that a slightly enhanced metals abundance may be appropriate.

We also plot the ratio of C III] λ 1909 to Si III] λ 1892. This ratio is useful for constraining the density because these lines are produced under roughly the same physical conditions (e.g., Hamann et al. 2002), yet they have different critical densities ($3.4 \times 10^9 \text{ cm}^{-3}$ and $1.04 \times 10^{11} \text{ cm}^{-3}$). As seen in Fig. 7, there seems to be some dependence on the flux (and therefore ionization parameter) as well.

For the high-ionization lines, seen in Fig. 7, we find that there is a region in which the contours of all of the lines are close to one another near $\log(\Phi) = 18.5$, and $\log(n_H) = 9.7$, which corresponds to $\log(U) \approx -1.7$. The contours show that the peak of the C IV emission lies in this region, while O VI, N V and He II peak at higher photon fluxes.

For the intermediate- and low-ionization lines, seen in Fig. 7, there is a region in which contours of all of the lines are close to one another near $\log(\Phi) = 18.2$, and $\log(n_H) = 9.7$, which corresponds to $\log(U) = -2$. The contours show that the peak of the C III] λ 1909 and C III λ 977 emission lies in this region, while C II, O III], Si III], and Mg II peak at slightly lower fluxes.

The rectangles showing the location of the best solutions for strongest high-ionization lines (Fig. 7) and the strongest intermediate- and low-ionization lines overlap in a region in which the ionization parameter lies in the range $-2.35 < \log(U) < -1.65$, and in which the density is $\log(n_H) = 9.75$. Thus, we demonstrate that the line emission in RE 1034+39 is consistent with emission from gas with uniform properties, as is suggested by the similar line profiles, and is consistent with illumination of that gas by the observed extreme spectral energy distribution.

4. Locally Optimally Emitting models

AGN monitoring campaigns have shown that emission line fluxes vary in response to continuum flux changes, with different lag times that depend primarily on the ionization potential of the line. This means that the broad-line region is in general radially stratified. Baldwin et al. (1995) proposed that perhaps the quasar emission line region is filled with clumps of gas of differing densities and distances from the source of the ionizing continuum. If this were the case, emission lines would naturally be produced over an extended region, peaking where the conditions for their emission are optimal. This is known as the Locally Optimally Emitting Cloud model, or LOC model. We note that there is evidence in some cases that the emission region is truncated in extent, ionization, or column density. For example, double-peaked broad line radio galaxies require truncation at the outer edge of the disk to create double peaks (Eracleous & Halpern 2004). In addition, the lack of intermediate- and low-ionization line emission in the broad blueshifted lines in some NLS1s required truncation of the column density in the wind component (Leighly 2004). Nevertheless, the LOC presents an arguably more physically realistic scenario than the one-zone model presented above.

In this section, we present our second photoionization analysis: an LOC model for RE 1034+39. At the same time, we recompute the LOC model using the parameters from Baldwin et al. (1995) for comparison. We first describe the assumptions of the model, and our scheme for integration, before describing the results.

4.1. Setting up the LOC model

Individual clouds are modeled with the same parameters used by Baldwin et al. (1995). Specifically, each single cloud has a hydrogen column density of $N_H = 10^{23} \text{ cm}^{-2}$, and is characterized by a single value of hydrogen density n_H and photon flux Φ . In order to reproduce Baldwin et al. results, we do not use N_H^{max} for the column density, as described above. A single column density for all clouds is a good assumption as long as all clouds are optically thick to the continuum. Following Baldwin et al., we discuss the results in terms of line ratios, and therefore the covering fraction does not enter into our calculations. We use solar abundances.

We ran the LOC models for two spectral energy distributions. We use the one we inferred for RE 1034+39, described in §2.6. For comparison, we also compute models for

the one used by Baldwin et al. (1995) that has a bump that peaks at 48 eV⁶. We computed a grid of models for each continuum over the same range of parameters used by Baldwin et al. (1995): density $8 < \log n < 14$ with $\Delta \log n = 0.125$ (cm⁻³); photon flux $18 < \log \Phi < 23$ with $\Delta \log \Phi = 0.125$ (photons cm⁻² s⁻¹).

4.2. Distribution Function and Integration

We follow Baldwin et al. (1995) to construct our LOC models. The emission line strengths in LOC models are computed by first assuming a function for the distribution of clouds in the density/photon flux plane, then using this as a weighting function to integrate over the line emission obtained from the grid with the following integral, which gives the luminosity of each line L :

$$L = \int r^2 F_{line}(r, n) \Psi(r, n) dr dn. \quad (1)$$

The *Cloudy* models yield the line flux at each value of (n_H, Φ) . The photon flux is related to the radius by $r \propto \Phi^{-1/2}$, and $F_{line}(r, n)$ is the line flux from the *Cloudy* models. $\Psi(r, n)$ is the distribution function. It is assumed to be a separable function of radius and density, so that $\Psi(r, n) = f(r)g(n)$. We use a power law for the distribution functions, so that $f(r) = r^\alpha$ and $g(n) = n^\beta$. Because the *Cloudy* grids are a function of Φ rather than of r , it is convenient to express $f(r)$ as a function of Φ instead. Using the assumption that $r \propto \Phi^{-1/2}$, $dr \propto \Phi^{-3/2}d\Phi$, and $d(\log \Phi) \propto d\Phi/\Phi$, we find that $f(\Phi) \propto \Phi^{-(\alpha+1)/2}$.

In order to obtain the integrated line emission, we use a two-dimensional integration scheme employing the trapizoidal method over the grid that is uniform in $d(\log n)$ and $d(\log \Phi)$. This method requires us to determine a weight for each grid point from the distribution functions. The result is $w_{ij} = C \times \Phi_i^{-(\alpha-1)/2} n_j^{\beta+1}$, where $C = 1$ for the interior of the grid, is $1/2$ for the edges, and is $1/4$ for the corners.

For each line, F_{ij} is the line flux from the *Cloudy* model, and C_{ij} is the monochromatic continuum flux under Ly α at every grid point (i, j) . Thus, the value F_{ij}/C_{ij} is proportional to the equivalent width. To compute the integral, we sum the weights over the grid as follows:

⁶In the *Cloudy* parameter file, this model is specified by “AGN T=800000,-1.4,-0.3,-1.0”

$$L \propto \sum_i \sum_j \frac{F_{ij}}{C_{ij}} w_{ij} d \log n d \log \Phi. \quad (2)$$

Using these values of the line luminosity L for each line we can compute the ratio of each line with Ly α .

4.3. LOC results

The ratios of the line fluxes to Ly α are given in Table 5 for both the RE 1034+39 and the *Cloudy* AGN continuum. We adopted the distribution functions used by Baldwin et al. (1995) in order to compare explicitly with their results ($f(r) = r^\alpha$ with $\alpha = -1$; $g(n) = n^\beta$ with $\beta = -1$). Note that Baldwin et al. (1995) erroneously report that they used $f(r) = \text{constant}$ and $g(r) \propto n^{-1}$ (Korista 2003, p. comm.)

We first verify that we can reproduce the Baldwin et al. (1995) results. The results taken directly from Baldwin et al. (1995) are given in column 2, and our re-creation of those results is given in column 3. We find slight differences due to the difference in versions of *Cloudy*; their computations were carried out with Version 90.02d, while ours were done with Version 94.00.

In column 4 we give the results from the RE 1034+39 SED, and, for comparison, the measured values from the spectra in column 5. While we are not able to match the line ratios exactly, the trends that we find are encouraging. That is, lines that are stronger with respect to Ly α in the RE 1034+39 LOC model compared with the AGN continuum LOC model are also stronger in the data. These include O VI+Ly β , N V, O IV]+Si IV, C IV, and O III]+He II. It is notable that the highest ionization line that we measure, O VI, is much stronger in both the data and the RE 1034+39 SED model than in the AGN LOC model. This fact verifies our expectation that the extremely hard SED should yield strong high ionization lines. Generally speaking, an extremely hard SED should create stronger collisionally-excited emission lines, because each ionizing photon carries more energy on average.

The largest differences between the ratios predicted by the LOC model for RE 1034+39 and the measured ratios are for C IV, for which the model predicts about twice the observed value, and in both cases, the values are larger than those from the AGN continuum. A very large discrepancy is found for Mg II, where the model predicts about five times the observed value, and the observed value is less than that predicted from the AGN continuum. This discrepancy might have been larger had we integrated to lower flux values in the LOC

computation, as Mg II is optimally emitted at $\log(\Phi) \sim 17$ (e.g., Korista et al. 1997). We have noticed that *Cloudy* models seem to frequently overpredict Mg II fluxes; a similar overprediction by about a factor of two was found in models for windy NLS1s given in Leighly (2004).

In Fig. 8, we show the line emissivity as a function of photon flux, assuming a 2-d geometry, for both the RE 1034+39 continuum, and the AGN continuum. In other words, we show the flux expected in each ring of area $2\pi r^2 dr$. The emissivity has been normalized by the luminosity in the entire line; i.e., we plot $L(R)/L_{total}$ for each line. For both continua, we see that significant line emission is predicted for the LOC model for fluxes lower than $\log \Phi \leq \sim 22$, out to at least $\log \Phi = 18$. However, the velocity widths of the lines may not support such a broad emission region. Assuming Keplerian velocities, a C IV velocity width of 900 km s^{-1} (Table 3), and an O VI velocity width of 1300 km s^{-1} corresponds to a ratio of fluxes of 4.4 at the radii where these lines should dominate, or $\Delta \log \Phi \approx 0.6$. This is a much smaller difference than the difference in the peaks of the C IV and N V distribution of $\Delta \log \Phi \approx 2.0$.

It is also interesting to note that the distribution of line emission is not much different for the two continua. The peaks for the higher-ionization lines are at slightly larger radii for RE 1034+39, except for C IV. The emissivity as a function of photon flux for Mg II is indistinguishable for the two SEDs. Another interesting thing about this plot is that the intermediate- and low-ionization lines increase strongly at larger radii (low flux). As discussed by Baldwin et al. (1995), the LOC model assumes truncation of line emission at $\Phi < 18$ as a result of graphite grains that will form in the clouds and decrease the emissivity. However, the steep increase in emissivity at larger radii predict that the observed flux of these intermediate- and low-ionization lines will depend very sensitively on the precise radius at which dust starts to dominate. This sensitivity possibly conflicts with the observation that the equivalent widths of these lines don't vary very much from object to object.

5. Exploring the Influence of the Spectral Energy Distribution

In §3 we presented photoionization models using the RE 1034+39 SED, and found that there is a region in the Φ/n plane that can roughly reproduce the equivalent widths of the lines that we measured. In §4, we presented an LOC model using the RE 1034+39 continuum, and noted differences in predicted emission lines from the relatively hard RE 1034+39 and the softer AGN continuum that correspond to our expectation that a hard continuum should produce stronger high-ionization lines, and a hard continuum should produce stronger collisionally-excited emission lines.

In this section, we present the third type of photoionization analysis: we wish to determine whether the emission lines in RE 1034+39 are not only consistent with its observed hard SED, but actually require it. That is, is it possible to produce the observed emission lines with a much softer SED, for some combination of ionization parameter and density? At the same time, we want to examine the influence of the shape of the spectral energy distribution on the emission lines in a more general way, for several reasons. First, the only other systematic investigation of BLR emission-line dependence on SED that we are aware of is Krolik & Kallman (1988), who consider only three distinct SEDs, and a handful of lines. We want to consider a larger range of SEDs and a larger number of lines. Furthermore, we are also planning to use this in further investigations of the influence of the SED on emission lines (in, e.g., PHL 1811, an object with a relatively soft SED; Leighly et al. in prep.). Finally, we use these results to investigate whether line ratios currently commonly used as density and metallicity indicators are sensitive to the SED. However, so that the flow of our discussion of the properties of RE 1034+39 is not interrupted, we relegate most of this discussion to the Appendix (§7). Briefly, we created a set of semiempirical spectral energy distributions parameterized by the cutoff temperature of the big blue bump kT_{cut} , which is measured in eV . We then used *Cloudy* (Version 96) to construct a grid of model line fluxes for a range of densities and ionization parameters. We calculate *a posteriori* (see §7.4) the effect of the global covering fraction.

5.1. Constraints using the RE 1034+39 Emission Lines

Using the results presented in the Appendix, we can now address the question: is the hard spectral energy distribution that we observed from RE 1034+39 required in order to generate the observed emission-line properties? In order to address this question, we follow a procedure similar to that used in Leighly (2004) to constrain *Cloudy* models for extreme NLS1s. We compare the line measurements from the observed spectra with the modeled line fluxes from the grids of *Cloudy* models using a figure of merit (*FOM*), defined as the absolute value of the difference of the base-10 log of the *Cloudy* line fluxes, transformed to the value that would be measured on Earth using the procedure described in the Appendix §7.4, and the observed line fluxes. Note that in Leighly (2004) the *FOM* was defined in terms of the line equivalent widths. Line fluxes work better here because the shape of the continuum underneath the lines changes as the SED changes; in Leighly (2004) that continuum was held constant. Thus the *FOM* is defined as

$$FOM_{jkm} = \sum_i |\log(F_{here,ijklm}^{model}) - \log(F_{here,i}^{measured})| \quad (3)$$

where i, j, k, m , and l index the individual lines, the kT_{cut} describing the SED, the $\log(U)$, the $\log(n_H)$, and the covering fraction, respectively.

The *FOM* is defined using O VI $\lambda 1034$, N V $\lambda 1240$, C IV $\lambda 1549$, He II $\lambda 1640$, C III] $\lambda 1909$, and Si III] $\lambda 1892$. These are the six highest-equivalent-width lines measured in RE 1034+39, excluding Ly α , which we discuss below, and the low-ionization line Mg II. As discussed in §7.3, the semiforbidden lines C III] and Si III] are commonly used as density indicators, and thus allow us to constrain the density in the line emitting gas in RE 1034+39.

We computed the *FOM* for the entire grid of *Cloudy* models. The minimum value of the *FOM* located the spectral energy distribution, ionization parameter, density and covering fraction that yielded line fluxes that matched most closely the observed fluxes. In Leighly (2004), evidence for multiple minima was found, so here we looked for multiple minima in a brute force way by sorting the data in order of increasing *FOM* and looking for jumps in the parameter values that would indicate another minimum. We also explored the *FOM* space by perturbing various parameters and examining the contours. After a thorough search, we found no evidence for multiple minima.

The minimum *FOM* was found for the following parameters: $kT_{cut} = 240$ eV, $\log(U) = -1.8$, $\log(n_H) = 9.125$ and a covering fraction of 6%. In Fig. 8, we show covering fraction/density, and $kT_{cut}/\log(U)$ cuts in *FOM* space around this minimum. It is important first to notice that the minima are somewhat broad; as discussed in Leighly (2004), broad minima are arguably physically more realistic because they imply that even though we are using a one-zone model, gas with properties perturbed a reasonable amount from the properties of the minimum will produce nearly identical lines so that the solution is not overly finely tuned. However, the *FOM* increases strongly toward lower kT_{cut} for values less than ~ 150 eV, indicating a harder SED is strongly favored.

Overlaid on Fig. 8 are the contours of the emission lines used to construct the *FOM*. We can see the confluence of the contours near the *FOM* minimum. The grid of models described in the Appendix only include $\log(U) \leq -1.125$, so we originally could not see if there were any other minima at higher ionization parameters. So we extend, for the best fitting values of the covering fraction and density, the $\log(U)$ vs kT_{cut} plane to higher values of $\log(U)$. Note that there is little density dependence for $\log(n_H) < 11.0$ for the high-ionization resonance lines, and, everything else being equal, the covering fraction only influences the flux, so we lose nothing by not considering those two parameters explicitly here. This extension reveals that the contours illustrating the measured values of the highest ionization lines (O VI, N V, and He II) do not dip below $kT_{cut} = 110$ eV. This indicates that a high kT_{cut} SED is supported even at high ionization parameter, and that perhaps the SED/ $\log(U)$ degeneracy is broken.

Our model, however, is not without limitations. In Fig. 9 we show the log of the ratio of the observed data to the model at the *FOM* minimum, both for the strong lines used to generate the *FOM*, and Ly α , Mg II, Si IV λ 1397, and C III λ 977 as well. A prominent difference is seen for Ly α . One possible explanation for this difference is that the gas in RE 1034+39 has somewhat enhanced metallicity; our *Cloudy* models consider only solar metallicity gas. We note that we found no similar discrepancy for the LOC models. We also find prominent discrepancy for Mg II, such that the model value is much too strong. We find this also for the LOC models for RE 1034+39, as discussed in §4.3, and we have no explanation for this. Si IV appears to be somewhat too strong; this is a weaker line that is generally blended with O IV] λ 1404, and it may be that we prescribe too large fraction of the 1400Å feature to Si IV.

In addition, this is a one-zone model; it assumes that all the lines are produced by gas with uniform ionization parameter, density and covering fraction. As discussed earlier, this assumption may be fairly good for RE 1034+39 in particular, since the high- and intermediate-line profiles are very similar. But comparison of Fig. 8 and Fig. 9 for the highest ionization lines may indicate the weakness in this assumption. Specifically, at the best *FOM* point, we produce too much C IV and insufficient O VI, resulting in discrepant observed-to-model ratios in Fig. 9. This discrepancy may be alleviated in a stratified model if a somewhat higher ionization parameter for the high-ionization lines is used. Nevertheless, the fact that the contours for the high-ionization lines lie at high kT_{cut} regardless of the ionization parameter may indicate that even for a stratified model, a relatively hard SED is still supported.

6. Discussion

6.1. Summary of Results

We have presented spectra and analysis from simultaneous *FUSE*, *ASCA*, and *EUVE* observations of the Narrow-line Seyfert 1 Galaxy RE 1034+39. Reanalysis of archival *HST* spectra were also presented. We find that almost all the lines in RE 1034+39 can be described well by narrow (FWHM $\leq \sim 1200$ km s $^{-1}$) Lorentzian profiles centered at the rest wavelength. That this is true for the UV emission lines was previously reported from the *HST* spectra by Puchnarewicz et al. (1998); our *FUSE* spectrum reveals for the first time the strong, narrow O VI line. The line profiles in RE 1034+39 are different than those in some other Narrow-line Seyfert 1 galaxies, in which only the intermediate- and low-ionization lines are narrow and centered at the rest wavelength; the high-ionization lines are broad and strongly blueshifted (e.g., Leighly & Moore 2004). Our simultaneous far-UV and X-ray observations

reveal a spectral energy distribution that peaks in soft X-rays, as was previously found by Puchnarewicz et al. (1995). This spectral energy distribution is much harder than that from typical quasars.

We presented three complementary types of photoionization analysis. First, we use the observed RE 1034+39 spectral energy distribution, and assume that because the emission lines all have very similar profiles, they all may be emitted by gas with approximately uniform ionization parameter and density. The presence of low-ionization emission lines implies that the gas is optically thick to the continuum. The ratio of the semiforbidden lines C III] and Si III] constrains the density of the gas to be around $\log(n_H) = 9.75$. The equivalent widths of the other strong emission lines are consistent with a photon flux of $\log(\Phi) \approx 18.4$, implying an ionization parameter near $\log(U) = -1.8$.

As has been discussed by Baldwin et al. (1995; see also Korista et al. 1997), the line-emitting gas may not be characterized by a single ionization parameter and a single density but rather there may be a distribution of gas properties, with the emission of any particular region being dominated by emission from lines most favorably produced there; this is the Locally Optimally-emitting Cloud or LOC model. The second photoionization analysis presented is an LOC model for RE 1034+39. We computed the ratios of the emission lines with Ly α for LOC models using the RE 1034+39 SED and gas and density distributions used previously by Baldwin et al. (1995). For comparison, we reproduce the Baldwin et al. results. We find that the LOC results correspond quite well with the observations from RE 1034+39. In particular, O VI is strong, as observed. An exception is Mg II, which is observed to be about 5 times weaker than predicted by the model.

Finally, we investigated the role of the spectral energy distribution on the emission line fluxes explicitly by constructing a set of semiempirical spectral energy distributions parameterized by the cutoff temperature of the blue bump, and computing a large grid of line fluxes as a function of density, ionization parameter, and spectral energy distribution. Following Leighly (2004), we define a figure of merit (*FOM*) as the sum of the absolute value of the difference between the model and observed fluxes for six strong emission lines. We find a fairly broad minimum in the *FOM* around $kT_{cut} = 240$ eV, $\log(U) = -1.8$, $\log(n_H) = 9.125$, and covering fraction of 6%. The RE 1034+39 continuum most closely matches a semi-empirical SED with $kT_{cut} \sim 230$ eV, so it is not surprising that the minimum *FOM* solution has nearly the same ionization parameter and density as was inferred in the photoionization analysis using the observed RE 1034+39 continuum. Furthermore, the *FOM* increases strongly toward lower values of kT_{cut} corresponding to softer continua, indicating that a hard continuum, in the context of a one-zone photoionization model, is necessary to produce the emission lines that we see; softer continua simply do not produce the strong

high-ionization lines that are the notable feature of the RE 1034+39 spectrum.

6.2. The O VI Line in RE 1034+39

In this section, we compare the O VI observed in RE 1034+39 with that observed in other AGN. RE 1034+39 is a somewhat exceptional object compared with most of those objects that have O VI measurements in that it has a relatively low luminosity, and a hard spectral energy distribution characterized by a flat α_{ox} . Such a hard spectral energy distribution is conducive for strong O VI emission; does RE 1034+39 match this expectation?

Zheng, Kriss & Davidsen (1995; hereafter ZKD) find a significant anticorrelation between the O VI/Ly α ratio and α_{ox} in a sample of quasars observed on the ground or with *HST*, *IUE*, or *HUT*. They present a regression for this anticorrelation: $\log(\text{O VI}/\text{Ly}\alpha) = -0.74\alpha_{ox} + 0.38$. Based on our measured $\alpha_{ox} = 1.22$, this regression predicts that O VI/Ly α will be 0.3.

We only measure the 1032Å component of O VI. Under optically-thin conditions, the ratio of the 1032Å component to the 1037Å component is 2.0. Under very optically-thick conditions, that ratio would be 1.0. Using the values for the line fluxes in Table 3, this analysis indicates a O VI/Ly α ratio between 0.76 and 1.0. So, the O VI flux relative to Ly α appears to be particularly large compared with other objects, and it can be seen from their Fig. 1 that this ratio would have been the largest in the ZKD sample. However, the regression of ZKD has uncertainties representing the spread in values; taking into account the uncertainties shows that the observed ratio can be explained. In addition, there are some differences in the way the data were analyzed. We detect O V] λ 1218, and our model removes that contribution from the Ly α flux. That was not done in the Zheng et al. sample, making their values of Ly α slightly larger, and hence their values of O VI/Ly α slightly smaller. However, if we combine our measured fluxes for Ly α and O V, it changes our ratio range to 0.59–0.78, still large compared with the rest of the ZKD sample.

Zheng, Kriss & Davidsen (1995) also compare the equivalent width of the objects in their sample with the UV monochromatic luminosity. Using their cosmology ($H_0 = 50 \text{ km s}^{-1} \text{ Mpc}^{-1}$; $q_0 = 1$) we find that $\log(L_{1550}) = 28.1 \text{ [erg s}^{-1}\text{]}$ for RE 1034+39. This value makes RE 1034+39 less luminous than all but one of the objects considered by Zheng et al. Using their regression for the anticorrelation between the O VI EW and the luminosity, we find a predicted O VI equivalent width of 150Å. The observed equivalent width of O VI λ 1032 component is 29Å, implying the equivalent width of the whole feature is between 43 and 58 Å. So, the predicted equivalent width is higher by greater than a factor of two.

Considering the regression is between logarithmic quantities, the discrepancy is probably acceptable. Furthermore, our observed equivalent widths are consistent with the range of equivalent widths implied by the uncertainties on the regression parameters.

We conclude that, although RE 1034+39 has extreme O VI properties, they are consistent with trends appropriate for an object with its observed spectral energy distribution and luminosity. This suggests that neither the emission line region geometry nor the inclination angle is especially unusual in this object, but rather is an extension of those in other quasars.

6.3. Directly Comparable Previous Results

Krolik & Kallman (1988) were possibly the first to address the issue of the response of various emission lines to the shape of the spectral energy distribution, with the aim of trying to determine the shape of the continuum in the unobservable extreme ultraviolet. They consider three spectral energy distributions that are different in the shape of the extreme UV. They compute emission line ratios for combinations of three ionization parameters and three pressures, finding that some ratios vary negligibly between the different SEDs, while some ratios show considerably greater range. They attribute these results to some extent to the relative strength in the continuum bands responsible for exciting production of particular emission lines. For example, He II $\lambda 1640$ and O VI are sensitive to the helium continuum, and therefore tend to be stronger with respect to Ly α for SEDs with strong helium continuum compared with Lyman continuum.

In the Appendix, we present similar computations as were presented by Krolik & Kallman (1988). A difference is that we examine a much larger range of spectral energy distributions and ionization parameters, although we do limit ourselves to discussion of a single density and slabs that are optically thick to the continuum in this paper. Another difference is that we examine a larger number of lines. Our inferences are more or less the same for our harder continua (§7.2). However, our results are somewhat different for the very soft continua that were not investigated by Krolik & Kallman (1988). For these continua, the low-ionization lines, which are produced below the hydrogen ionization front for the harder continua, are produced above the hydrogen ionization front and become primary coolants. While not directly applicable in this paper, the results of low-kT simulations are important for understanding objects with soft continua such as PHL 1811 (Leighly et al. in prep.)

We thank Jules Halpern for reducing the *EUVE* data, and we thank Chiho Matsumoto for reducing the *ASCA* data. DC acknowledges helpful discussions with John Moore, and with Kirk Korista regarding the LOC models. We thank Joe Shields for suggesting the

identification of O V λ 1218. We acknowledge useful comments from an anonymous referee that resulted in substantial improvement in the paper. Some of the data presented in this paper were obtained from the Multimission Archive at the Space Telescope Science Institute (MAST). STScI is operated by the Association of Universities for Research in Astronomy, Inc., under NASA contract NAS5-26555. Support for MAST for non-HST data is provided by the NASA Office of Space Science via grant NAG5-7584 and by other grants and contracts. This research has made use of the NASA/IPAC Extragalactic Database (NED) which is operated by the Jet Propulsion Laboratory, California Institute of Technology, under contract with the National Aeronautics and Space Administration. This research has made use of data obtained from the High Energy Astrophysics Science Archive Research Center (HEASARC), provided by NASA’s Goddard Space Flight Center. KML and DAC gratefully acknowledge support by NASA grants NAG5-10171 (LTSA), NAG5-10038 (FUSE), and NAG5-10366 (FUSE). EB gratefully acknowledges partial support by NASA grants NAG5-3505 and NAG5-12127, NSF grant AST0204771, and computer resources at NERSC supported by the US DOE.

7. Appendix

7.1. Photoionization Modeling with a Semi-Empirical SED

To test the influence of the spectral energy distribution on the line emission, we needed a series of SEDs that could be expressed simply mathematically, and yet are approximately physically realistic. We start with the AGN spectrum that is included in the *Cloudy* package:

$$f_{\nu} = \nu^{-\alpha_{uv}} e^{\frac{h\nu}{kT_{cut}}} e^{\frac{kT_{IR}}{h\nu}} + a\nu^{\alpha_x}. \quad (4)$$

This equation models the big blue bump as a power law with index α_{uv} in the optical and UV with an exponential cut off at high energies parameterized by the temperature T_{cut} , and an exponential cutoff at low energies parameterized by T_{IR} . A power law with index α_x models the X-ray spectrum. We fixed the optical/UV power law index to $\alpha_{uv} = 0.33$, adopting the observationally-determined mean value from a sample of quasars by Natali et al. (1998), which is in agreement with the mean obtained from the LBQS by Francis et al. (1991), and with the Einstein sample from Elvis et al. (1994). We fixed the X-ray power law continuum slope to $\alpha_x = 1$ (e.g., Zdziarski, Poutanen, & Johnson 2000).

For the thin disk model, the high energy cutoff for the optical-UV continuum is theoretically related to the temperature of the inner edge of the accretion disk. For a fixed

accretion rate with respect to the Eddington value, and for a fixed efficiency of conversion of accretion energy to radiation, we expect the accretion disk luminosity to be proportional to T^{-4} . The relative normalization between the X-ray and UV is observed to be dependent on luminosity through α_{ox} , the point-to-point slope between 2500Å and 2 keV (Wilkes et al. 1994). We use the theoretical constraint provided by the inner edge temperature, and the empirical constraint provided by the α_{ox} to relate T_{cut} to the X-ray power law normalization a through their mutual dependence on luminosity. The proportionality constant was determined using the measured T_{cut} from coordinated *IUE* and *ROSAT* observations of the quasar 3C 273 (Walter et al. 1994). Our final constraint relates the lower limit frequency of the X-ray power law to T_{cut} so that the power law cannot be discerned in the optical-UV band.

In the discussion that follows, the spectral energy distribution is uniquely parameterized by the value of kT_{cut} . We computed photoionization models for a range of kT_{cut} from 10 eV to 320 eV, with $\Delta kT_{cut} = 10$. A representative subset of the spectral energy distributions, normalized so that they all have the same ionizing flux, are shown in Fig. 11. As shown in Fig. 12, a spectral energy distribution with $kT_{cut} = 230$ eV coincides fairly well with the spectral energy distribution of RE 1034+39, and one with $kT_{cut} = 10$ eV corresponds well with that of PHL 1811, a luminous NLS1 (Leighly et al. 2001; Leighly, Halpern & Jenkins 2004; Leighly et al. in prep.). This demonstrates that these semiempirical SEDs are representative of observed SEDs.

Our primary goal is to determine whether the emission lines in RE 1034+39 require a hard spectral energy distribution, or whether they are independent of SED. Thus, we choose the remaining parameters for the photonization models to be appropriate for RE 1034+39. In §3 we found that the column density should be large enough to be optically thick to the continuum. Therefore, here we use $N_H^{max} = 25$, which is sufficiently thick to produce low-ionization lines such as C II. We verified that, for a fixed ionization parameter, the depth of the hydrogen ionization front is almost independent of the shape of the spectral energy distribution (Fig. 13). However, the depth of the helium ionization front changes, being deeper for harder SEDs (Fig. 13). This trend is expected, as a larger proportion of the ionizing photons are in the helium continuum for harder SEDs.

We run *Cloudy* models for SEDs with $10 < kT < 320$; $\Delta(kT) = 10$, for hydrogen densities $7.875 < \log(n_H) < 12.75$; $\Delta(\log(n_H)) = 0.125$, and for ionization parameters $-3.0 < \log(U) < -1.25$; $\Delta(\log(U)) = 0.125$. Thus, 19,200 models were considered.

$\text{Ly}\alpha$ is a recombination line, and its intensity will depend primarily on the depth of the hydrogen ionization front for the fixed density considered in these models. Thus, its intensity should depend *only* on the ionizing flux, which is proportional to the ionization parameter

for a fixed density, and be independent of the shape of the continuum, as long as the density is not so high that it starts to become thermalized. The contours of Ly α flux as a function of ionization parameter and kT_{cut} show that this is indeed the case (Fig. 14). Therefore, to partially remove the effect of the ionization parameter, we present the results as ratios of lines with respect to Ly α .

7.2. Model Results

In this discussion, we consider only the dependence on the spectral energy distribution and ionization parameter, and consider only one density, $n_H = 10^{10} \text{ cm}^{-2}$. Fig. 15–18 shows contours of emission lines with respect to Ly α for the adopted range of kT_{cut} and ionization parameter. We divide the results into four categories based on the ionization potential of the emitting ion and the emission mechanism. Figures 15–17 show the predominately collisionally excited lines, with Fig. 15 showing lines with ionization potential (I.P.) greater than that of He II (I.P. $> 54.4 \text{ eV}$), Fig. 16 showing lines with I.P. between that of hydrogen and helium ($13.6 < \text{I.P.} < 54.4$), and Fig. 17 with I.P. less than that of hydrogen (I.P. $< 13.6 \text{ eV}$). Fig. 18 shows recombination lines from hydrogen and helium.

The behavior of some lines is quite easy to understand. For example, Fig. 15 shows the emission lines from ions with ionization potential higher than that of He $^{2+}$. They are emitted most strongly when the continuum is relatively hard, because the ionization potential of the ions that create these lines is relatively high. They are emitted strongly when the ionization parameter is high because a high ionization parameter is required for the high ionization state. In addition, the harder continuum generates a higher temperature in the gas. The lines shown here are those from transitions with low excitation potentials, and are thus primary gas coolants. Therefore, the contours shown in Fig. 15 have maxima along the top of the plot, where the continuum is hard, and tail toward the right side, where the ionization is high.

Turning to Fig. 16, we find emission lines emitted between the helium ionization front and the hydrogen ionization front. In particular, C IV and N IV] are emitted most favorably at intermediate values of the ionization parameter, near $\log(U) = -1.5$. Again, these peak for the hardest continua because they are important gas coolants.

The situation is somewhat different for the intermediate ionization lines O III], Si IV, N III $\lambda 991$, N III] $\lambda 1750$, C III $\lambda 977$, and C III] $\lambda 1909$, shown in Fig. 16a. These lines are most favorably produced at somewhat lower ionization than the lines discussed above. Therefore, their contours peak along the top of the plots at slightly lower ionization parameter (e.g.,

$\log(U) \approx -2$ for C III). They also show enhancements along the right side of the plots for continua with intermediate hardness. This occurs because in this region of the plots, the continua are too soft to create abundant ions with highest ionization; intermediate ionization states are dominant above the hydrogen ionization front. This is a consequence of the reduction in depth from the illuminated side of the slab to the helium ionization front, and the corresponding increase in depth of the intermediate ionization region between the helium and hydrogen ionization fronts as the spectra become softer. Thus, at high ionization, the gas cools via production of intermediate ionization lines. The excitation of the ions is predominately collisional in both regions of the plots, so permitted and semiforbidden lines have roughly the same behavior.

The situation is radically different for the intermediate ionization lines Al III and Si III]. The contours from these lines, shown in Fig. 16b, peak at intermediate ionization parameter, but are stronger for the softer spectra. It is particularly interesting to note the differing behavior for C III] and Si III]; the contours shown in Fig. 16b are almost mutually exclusive. The ions responsible for these lines are isoelectronic. Both are transitions from the ground state to levels with the same configuration ($^3P^0$), and their excitation potentials are quite similar. The principle difference between them appears to be the ionization potential to create the +2 and +3 ions. To create Si^{2+} and C^{2+} , the ions emitting these lines, 16.4 and 24.3 eV are required, respectively. To ionize them to the +3 state, 33.4 and 47.9 eV are required, respectively. Thus, Si^{2+} is more favorably produced when the continua are soft; for harder continua, the predominate ionization state in the intermediate ionization region is Si^{3+} . Furthermore, the *Cloudy* output indicates that for $\log(U) \approx -2$ and for the softer spectra, Si III] is the predominant coolant. Al III behaves similarly, although it is a permitted line, as the ionization potentials to create Al^{2+} and Al^{3+} are 18.8 and 28.4 eV, respectively.

Moving to the low-ionization lines, we show contours from N II, C II, Si II, Al II, Mg II, Ca II, and Na I in Fig. 16b and 17. The contours from these lines exhibit different behavior. First we consider the pairs of lines of N II $\lambda 1085$, N II] $\lambda 2140$, and C II $\lambda 1335$, C II] $\lambda 2326$. In both cases, the semiforbidden line is most strongly emitted at low ionization parameter for a hard spectrum, while the permitted line is most strongly emitted at a high ionization parameter for a soft spectrum. Although these are low-ionization lines, they are emitted in the partially ionized zone only for the hard spectra and high ionization parameter. Examination of the *Cloudy* output shows that this contrasting behavior originates in different excitation of the ion in the two regimes. At low ionization parameter, the semiforbidden line is collisionally excited. For a particular ionization parameter, it therefore emits most strongly for the harder spectra because the gas temperature is higher. The permitted lines are weaker in this regime because they have much higher excitation potentials than the semiforbidden lines, and for the low ionization parameters at which the appropriate ions

exist, the temperature is not high enough to excite them. They are emitted more favorably for soft spectra at high ionization parameter as a result of recombination.

The behavior of the low-ionization line Si II is interesting. The Si⁺ ion has five groups of permitted resonance transitions with upper level energies less than 11 eV, near 1160, 1263, 1308, 1531 and 1814 Å. For harder continua, the *Cloudy* output indicates that the excitation is predominately collisional. Thus, the 1814 Å line is generally predicted to be the strongest of the Si II resonance lines, and is further predicted to be stronger relative to Ly α at the lowest ionization parameters. But for the softer spectra, continuum pumping is the predominate process for the higher excitation transitions. In fact, for the highest ionization parameter and softest spectrum, the higher-ionization transitions are as strong or stronger than Si II λ 1814. This is an interesting result, because while Si II λ 1263 and Si II λ 1308 are strong in some AGNs, Si II λ 1814 is not correspondingly strong, a result that has been difficult to explain (Baldwin et al. 1996). This issue will be examined further in Leighly et al. (2004 in prep).

We turn next to the low ionization lines from Mg⁺, Al⁺, Ca⁺, and neutral sodium (Fig. 17). These contours tend to be enhanced for the hardest and softest spectra. For the hardest spectra, these emission lines are produced to a large extent in the partially ionized zone beyond the hydrogen ionization front. The partially ionized zone is predominately powered by X-rays. As shown in Fig. 13, as the spectra become softer, the depth of the partially-ionized zone shrinks, resulting in relatively less emission at a given ionization parameter for spectra with intermediate hardness. For the softest spectra, these lines are again produced strongly, because the ions emitting these lines have low ionization potentials; thus these lines serve relatively larger role as cooling agents when the spectra are soft.

Finally, we consider the recombination lines from hydrogen and helium. The He II lines are relatively easy to understand. They are strong when the helium ionization front is deep. As seen in Fig. 13, this is true when the continuum is hard. In contrast, He I is strong when the region between the helium and hydrogen ionization fronts is large; as seen in Fig. 13, this condition is met when the continuum is relatively soft.

7.3. SED Dependence of the Density Diagnostic Si III]/C III]

The ratio of the semiforbidden lines Si III] and C III] is frequently used to estimate the density of the emitting gas. These emission lines are produced by isoelectronic ions and have similar but not identical excitation potentials, and therefore in principle should be produced under roughly the same conditions. The important difference is in their critical densities:

$1.04 \times 10^{11} \text{ cm}^{-3}$ and $3.4 \times 10^9 \text{ cm}^{-3}$ for Si III] and C III] respectively.

The analysis presented above shows, however, that these emission lines are not independent of the spectral energy distribution, as a consequence of their different roles in cooling the gas, which may be the consequence of the differing ionization potentials. As discussed above, for intermediate and soft spectra with ionization parameter of $\log(U) = -2.5$, Si III] is emitted strongly because it is one of the primary coolants for the gas; for harder spectra, the ions responsible for cooling are instead C^{3+} and Si^{3+} . Thus, a high Si III] to C III] ratio could either indicate high density, or a soft spectral energy distribution. This is illustrated in Fig. 19, which shows, for example, a range of greater than 2 in this ratio *for a fixed density and ionization parameter* near $\log(U) = -2.3$, as the SED varies from hard to soft. Thus, there is a degeneracy between density and spectral energy distribution for the Si III]/C III] ratio that in principle could hamper its use as a density indicator.

This degeneracy may be partially broken by using Al III in combination with Si III] and C III]. Al III is also predicted to be strong when the spectrum is soft, but it has little dependence on density because it is a permitted line. Thus, if both Al III and Si III] are strong with respect to C III], a soft spectrum may be indicated; if Al III is weak while Si III] is strong, a high density may be indicated.

7.4. SED Dependence of Metallicity indicators

We looked at the SED dependence for three different metallicity indicators (e.g., Hamann et al. 2002): N III $\lambda 1750$ /O III] $\lambda 1666$, N V $\lambda 1240$ /C IV $\lambda 1550$, and N V/(O VI+C IV) (Fig. 20). Fig. 20a shows that N III]/O III] has little dependence on the spectral energy distribution, and is therefore arguably the most reliable metallicity indicator. In contrast, Fig. 20b shows that the N V/C IV ratio has a strong dependence on ionization parameter, and some dependence on SED for the softest spectral energy distributions. The ionization parameter dependence is partially mitigated by using instead the N V/(C IV+O VI) ratio (Hamann et al. 2002) as shown in Fig. 20c, except for the softest SEDs.

7.5. Obtaining the Observed Model Line Fluxes for Comparison With Measured Values

For reference, in this section, we describe the method that we used to compare the *Cloudy* results with the observed line fluxes.

The luminosity of the ionizing light observed here on Earth equals the luminosity of the

ionizing light at the continuum source, i.e.,

$$L_{here} = L_{there}. \quad (5)$$

Therefore, if d equals the distance from the ionizing continuum source to the observer, Φ equals the number flux of ionizing photons from the continuum source, and r equal to the distance from the ionizing continuum source to the photoionized gas, we find that

$$\Phi_{here}d^2 = \Phi_{there}r^2, \quad (6)$$

so that

$$\frac{\Phi_{here}}{\Phi_{there}} = \frac{r^2}{d^2}. \quad (7)$$

If the clouds do not cover the ionizing continuum source completely, the covering fraction CF must be taken explicitly into account so that

$$r^2CF\Phi_{there} = d^2\Phi_{here}. \quad (8)$$

Eliminating the distances using Equation 7, and taking the base-ten log, we obtain

$$\log(\Phi_{here}) = \log(\Phi_{there}) - \log(CF) + \log(\Phi_{there}). \quad (9)$$

The figure of merit is defined as the absolute value of the difference in the base-ten log of the line fluxes, and is given by

$$FOM_{ijklm} = |\log(\Phi_{here}) - \log(\Phi_{there,k}) + \log(CF_l) + \log(F_{there,ijk}^{model}) - \log(F_{here,i}^{measured})| \quad (10)$$

where i, j, k , and m index the individual lines, the value of kT_{cut} , the value of $\log(U)$, and the value of $\log(n_H)$, respectively.

Assuming arbitrarily that $\log(\Phi_{there})$ is 17.75, then we can express $\log(\Phi_{here})$ as

$$\log(\Phi_{here}) = 17.75 - \Delta \log(\Phi), \quad (11)$$

where $\Delta \log(\Phi)$ is the scaling factor required to reduce the observed continuum with photoionizing flux of 17.75 to the photoionizing flux we observe on Earth. Comparing the *Cloudy* output with the observed spectral energy distribution indicates that $\Delta \log(\Phi) = 18.25$. Inserting Equation 11 in to the *FOM* equation results in

$$FOM_{ijkml} = |17.75 - 18.25 - \log(\Phi_{there,j}) + \log(CF_l) + \log(F_{there,ijkm}^{model}) - \log(F_{here,i}^{measured})|. \quad (12)$$

REFERENCES

- Baldwin, J. A., 1977, *ApJ*, 215, 408
- Baldwin, J. A., Ferland, G., Korista, K., & Verner, D., 1995, *ApJ*, 455, 119
- Baldwin, J. A., 1997, Proc. “Emission Lines in Active Galaxies: New Methods and Techniques”, eds. B. M. Peterson, F.-Z. Cheng, & A. S. Wilson (ASP: San Francisco) p. 80
- Baldwin, J. A., Ferland, G. J., Korista, K. T., Carswell, R. F., Hamann, F., Phillips, M. M., Verner, D., Wilkes, B. J., & Williams, R. E., 1996, *ApJ*, 461, 664
- Bechtold, J., Siemiginowska, A., Shields, J., Czerny, B., Janiuk, A., Hamann, F., Aldcroft, T. L., Elvis, M., & Dobzycki, A., 2003, *ApJ*, 588, 119
- Boroson, T. A., & Green, R. F., 1992, *ApJS*, 80, 109
- Brandt, W. N. & Boller, T. 1999, ASP Conf. Ser. 175: Structure and Kinematics of Quasar Broad Line Regions, 265
- Brotherton, M. S., Wills, B. J., Steidel, C. C., & Sargent, W. L. W., 1994, *ApJ*, 423, 131
- Brotherton, M. S., Tran, H. D., Becker, R. H., Gregg, M. D., Laurent-Muehleisen, S. A., & White, R. L., 2001, *ApJ*, 546, 775
- Brotherton, M. S., Green, R. F., Kriss, G. A., Oegerle, W., Kaiser, M. E. Zheng, W., & Hutchings, J. B., 2002, *ApJ*, 565, 800
- Cardelli, J. A., Clayton, G. C., & Mathis, J. S. 1989, *ApJ*, 345, 245
- Collin, S. & Joly, M. 2000, *New Astronomy Review*, 44, 531
- Collin-Souffrin, S., Dumont, S., & Tully, J. 1982, *A&A*, 106, 362
- Collin-Souffrin, S., Joly, M., Pequignot, D., & Dumont, S. 1986, *A&A*, 166, 27

- Collin-Souffrin, S., Dyson, J. E., McDowell, J. C., & Perry, J. J. 1988, MNRAS, 232, 5
- Czerny, B., Nikolajuk, M., Rozanska, A., Dumont, A.-M., Loska, Z., & Zycki, P. T., 2003, A&A, 412, 317
- Dietrich, M., Hamann, F., Shields, J. C., Constantin, A., Vestergaard, M., Chaffee, F., Foltz, C. B., & Junkkarinen, V. T., 2002, ApJ, 581, 912
- Elvis, M., Wilkes, B. J., McDowell, J. C., Green, R. F., Bechtold, J., Willner, S. P., Oey, M. S., Polomski, E., & Cutri, R., 1994, ApJS, 95, 1
- Elvis, M., et al. 1994, ApJS, 95, 1
- Eracleous, M. & Halpern, J. P. 2004, ApJS, 150, 181
- Espey, B. & Andreadis, S. 1999, ASP Conf. Ser. 162: Quasars and Cosmology, 351
- Ferland, G. J., 2001, “Hazy, a Brief Introduction to *Cloudy* 96.00”
- Ferland, G. J. & Persson, S. E. 1989, ApJ, 347, 656
- Francis, P. J., Hewett, P. C., Foltz, C. B., Chaffee, F. H., Weymann, R. J., & Morris, S. L., 1991, ApJ, 373, 465
- Frank, J., King, A., & Raine, D. J., 2002, *Accretion Power in Astrophysics: Third Edition* (Cambridge University Press)
- Gaskell, C. M., 1985, ApJ, 291, 112
- Green, P. J. 1996, ApJ, 467, 61
- Green, P. J., 1998, ApJ, 498, 170
- Green, P. J., Forster, K., & Kuraszewicz, J. 2001, ApJ, 556, 727
- Grupe, D., Beuermann, K., Thomas, H.-C., Mannheim, K., & Fink, H. H., 1998, A&A, 330, 25
- Halpern, J. P., Leighly, K. M., & Marshall, H. L., 2003, ApJ, 585, 665
- Hamann, F., Cohen, R. D., Shields, J. C., Burbidge, E. M., Junkkarinen, V., & Crenshaw, D. M. 1998, ApJ, 496, 761
- Hamann, F., Korista, K. T., Ferland, G. J., Warner, C., & Baldwin, J. 2002, ApJ, 564, 592

- Ho, L. C., 2003, in proc. “Active Galactic Nuclei: from Central Engine to Host Galaxy”, Eds. S. Collin, F. Combes, & I. Schosman (ASP) 379, astro-ph/0303059
- Korista, K., Baldwin, J., Ferland, G., & Verner, D., 1997, ApJS, 108, 401
- Korista, K., Ferland, G., & Baldwin, J. 1997, ApJ, 487, 555
- Korista, K., Baldwin, J., & Ferland, G., 1998, ApJ, 507, 24
- Kriss, G. A., 1994, in “Astronomical Data Analysis Software & Systems III, A.S.P. Conf. Series, Vol. 61”, eds. D. R. Crabtree, R. J. Hanisch, & J. Barnes (Astronomical Society of the Pacific: San Francisco), p. 437
- Kriss, G. A., 2001, in “Probing the Physics of Active Galactic Nuclei”, eds. B. M. Peterson, R. W. Pogge, & R. S. Polidan, (San Francisco: PASP), p. 45
- Krolik, J. H., & Kallman, T. R., 1988, ApJ, 324, 714
- Kuraszkiewicz, J., Wilkes, B. J., Czerny, B., & Mathur, S. 2000, ApJ, 542, 692
- Kwan, J. & Krolik, J. H. 1981, ApJ, 250, 478
- Laor, A., & Netzer, H., 1989, MNRAS, 242, 560
- Leighly, K. M., 1999, ApJS, 125, 317
- Leighly, K. M., 2004, ApJ, 611, 125
- Leighly, K. M., Halpern, J. P., Helfand, D. J., Becker, R. H., & Impey, C. D. 2001, AJ, 121, 2889
- Leighly, K., Halpern, J., & Jenkins, E. 2004, “AGN Physics with the Sloan Digital Sky Survey”, Eds. G. T. Richards & P. B. Hall (San Francisco: ASP), p. 277
- Leighly, K. M., & Moore, J. R., 2004a, ApJ, 611, 107
- Leighly, K. M., & Moore, J. R., 2004b, submitted to ApJ
- Moos, H. W., et al. 2000, ApJ, 538, L1
- Mukai, K., 1993, Legacy, 3, 21
- Murphy, E. M., Lockman, F. J., Laor, A., & Elvis, M., 1996, ApJS, 105, 369
- Murray, N., Chiang, J., Grossman, S. A., & Voit, G. M. 1995, ApJ, 451, 498

- Mushotzky, R. F., & Ferland, G. J., 1984, *ApJ*, 278, 558
- Natali, F., Giallongo, E., Cristiani, S., & La Franca, F., 1998, *AJ*, 115, 397
- Nussbaumer, H. & Storey, P. J. 1982, *A&A*, 115, 205
- Osmer, P. S., Porter, A. C., & Green, R. F. 1994, *ApJ*, 436, 678
- Osmer, P. S. & Shields, J. C. 1999, *ASP Conf. Ser.* 162: *Quasars and Cosmology*, 235
- Osterbrock, D. E., 1989 “*Astrophysics of Gaseous Nebulae and Active Galactic Nuclei*” (Mill Valley: University Science Books)
- Peterson, B. M., 1993, *PASP*, 105, 247
- Peterson, B. M., 1997, “*An Introduction to Active Galactic Nuclei*” (Cambridge University Press)
- Pounds, K. A., Done, C., & Osborne, J. P., 1995, *MNRAS*, 277, 5P
- Proga, D., & Kallman, T. R., 2004, *ApJ*, in press
- Proga, D., Stone, J. M., & Kallman, T. R. 2000, *ApJ*, 543, 686
- Puchnarewicz, E. M., Mason, K. O., Siemiginowska, A., & Pounds, K. A., 1995, *MNRAS*, 276, 20
- Puchnarewicz, E. M., Mason, K. O., & Siemiginowska, A., 1998, *MNRAS*, 298, L52
- Puchnarewicz, E. M., Mason, K. O., Siemiginowska, A., Fruscione, A., Comastri, A., Fiore, F., & Cagnoni, I., 2001, *ApJ*, 550, 644
- Romano, P., Mathur, S., Pogge, R. W., Peterson, B. M., & Kuraszkiewicz, J., 2002, *ApJ*, 578, 64
- Rózanska, A., & Czerny, B., 2000, *MNRAS*, 316, 473
- Rózanska, A., & Czerny, B., 2000, *MNRAS*, 360, 1170
- Ross, R. R., Fabian, A. C., & Mineshige, S., 1992, *MNRAS*, 261, 74
- Sahnou, D. J., 2000, *ApJ*, 538, L7
- Schlegel, D. J., Finkbeiner, D. P., & Davis, M., 1998, *ApJ*, 500, 525

- Scott, J. E., Kriss, G. A., Brotherton, M., Green, R. F., Hutchings, J., Shull, J. M., & Zheng, W., ApJ, in press
- Shakura, N. I., & Sunyaev, R. A., 1973, A&A, 24, 337
- Shang, Z., Wills, B. J., Robinson, E. L., Wills, D., Laor, A., Xie, B., & Yuan, J. 2003, ApJ, 586, 52
- Shang, Z, et al. 2005, ApJ, 619, 41
- Shull, J. M., Tumlinson, J. Giroux, M. L., Kriss, G. A., & Reimers, D., 2004, ApJ, 600, 570
- Soria, R., & Puchnarewicz, E. M., 2002, MNRAS, 329, 456
- Svensson, R., & Zdziarski, A. A 1994, ApJ, 436, 599
- Vignali, C., Brandt, W. N., Schneider, D. P., Anderson, S. F., Fan, X., Gunn, J. E., Kaspi, S., Richards, G. T., & Strauss, M. A., 2003, AJ, 125, 2876
- Walter, R., Orr, A., Courvoisier, T. J.-L., Fink, H. H., Makino, F., Otani, C., & Wamstecker, W., 1994, A&A, 285, 119
- Wandel, A. & Boller, T. 1998, A&A, 331, 884
- Wang, T., Lu, Y., & Zhou, Y. 1998, ApJ, 493, 1
- Warner, C., Hamann, F., & Dietrich, M. 2004, ApJ, 608, 136
- Wilkes, B. J., Tananbaum, H., Worrall, D. M., Avni, Y., Oey, M. S., & Flanagan, j., 1994, ApJS, 92, 53
- Wilkes, B. J., Kuraszewicz, J., Green, P. J., Mathur, S., & McDowell, J. C., 1999, ApJ, 513, 76
- Wills, B. J., Netzer, H., & Wills, D. 1985, ApJ, 288, 94
- Wills, B. J., Laor, A., Brotherton, M. S., Wills, D., Wilkes, B. J., Ferland, G. J., & Shang, Z. 1999, ApJ, 515, L53
- Zdziarski, A. A., & Gierlinski, M., 2004, Proc. of “Stellar-mass, Intermediate-mass, and Supermassive Black Holes”, astro-ph/0403683
- Zdziarski, A. A., Poutanen, J., & Johnson, W. N., 2000, ApJ, 542, 703
- Zheng, W., Kriss, G. A., & Davidsen, A. F. 1995, ApJ, 440, 606

Zheng, W., Kriss, G. A. Telfer, R. C. Grimes, J. P. & Davidson, A. F. 1997, ApJ, 475, 469

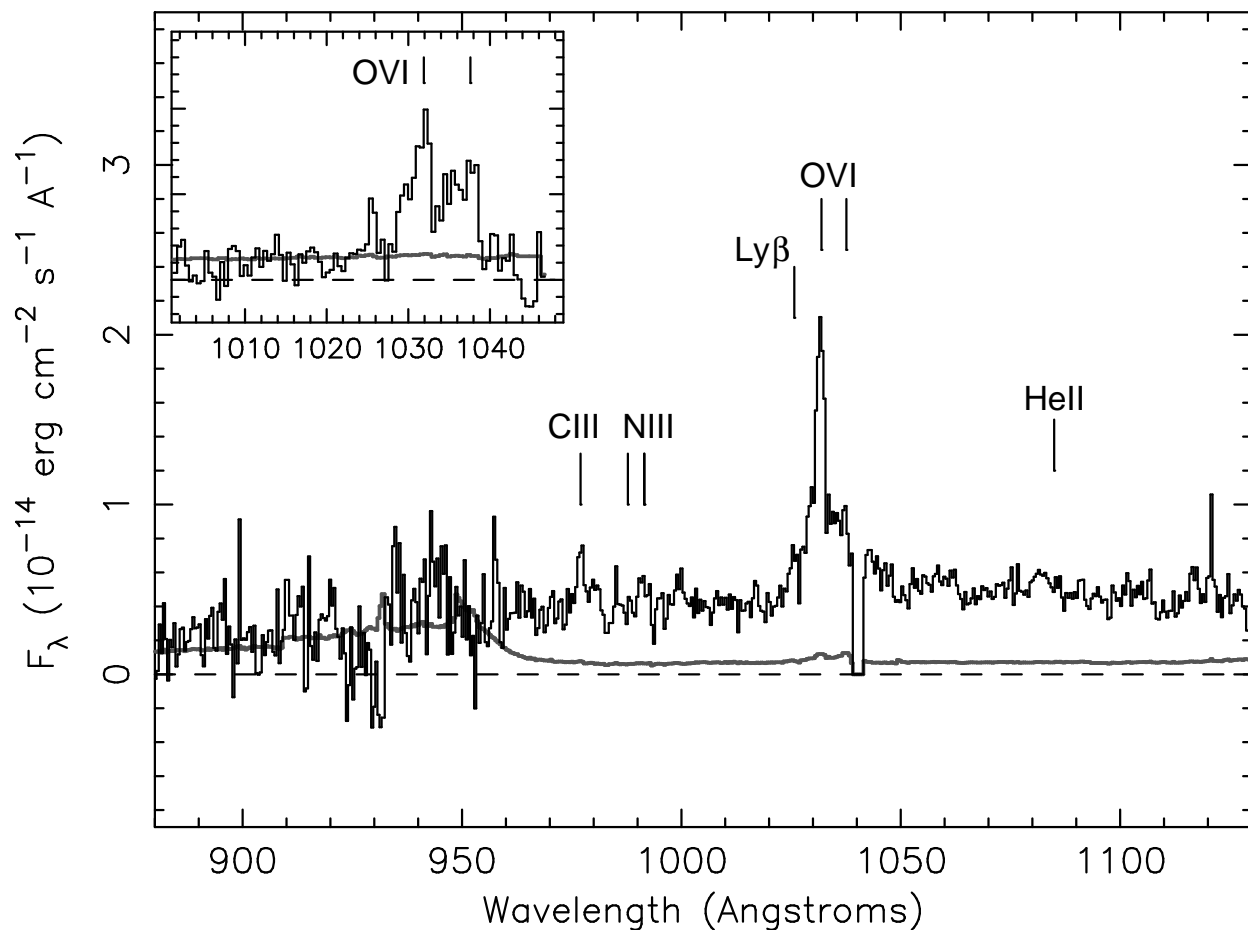


Fig. 1.— The extracted, coadded *FUSE* spectrum of RE 1034+39. Airglow lines from $\text{Ly}\beta$, $\text{Ly}\delta$, and $\text{Ly}\gamma$ have been removed. The thick line shows the uncertainty spectrum. Emission lines commonly observed in this bandpass in AGN are labeled; we detect C III, O VI, and $\text{Ly}\beta$. Note that the 1037 Å component of the O VI doublet was not detected in the LiF1a spectrum, as it falls on the edge of the detector where background is enhanced (see text for details). Inset: the SiC1a spectrum, showing enhancements at the appropriate wavelengths for both components of the O VI line.

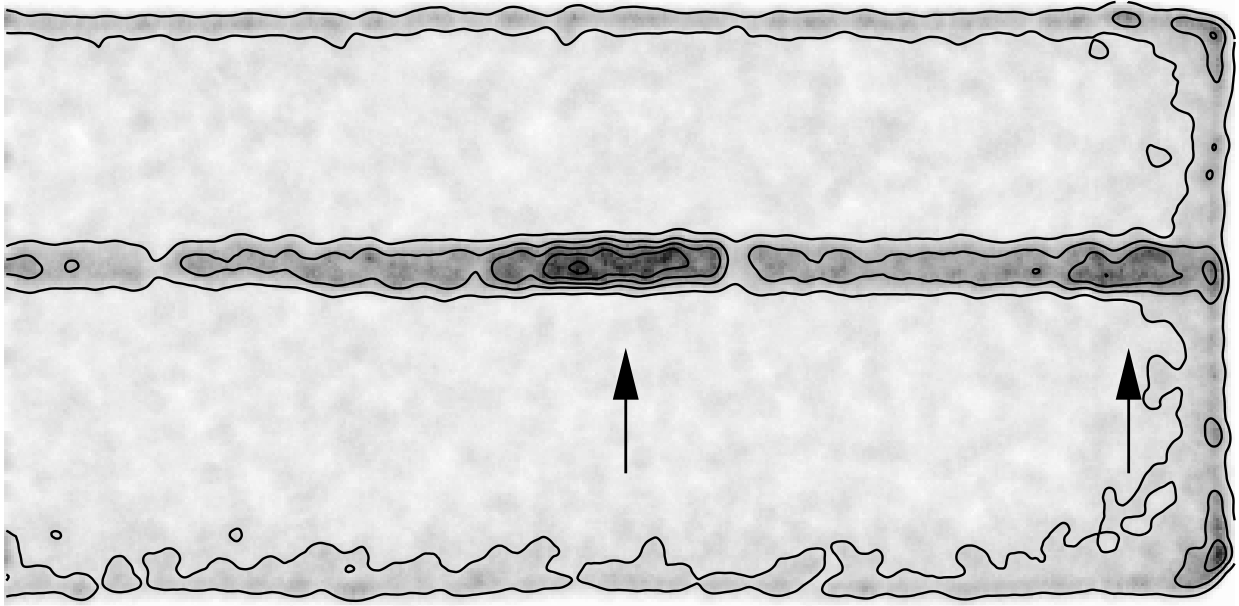


Fig. 2.— The long wavelength portion of the LIF1 detector image, after screening and before background subtraction. The image has been adaptively smoothed and is plotted on a linear scale. The LIF1a trace is clearly detected. The arrows show approximate expected centers of the O VI doublets. The 1031.93\AA component is clearly seen. The 1037.62\AA component can be seen near the edge of the detector, where the effective area is lower and the background is higher.

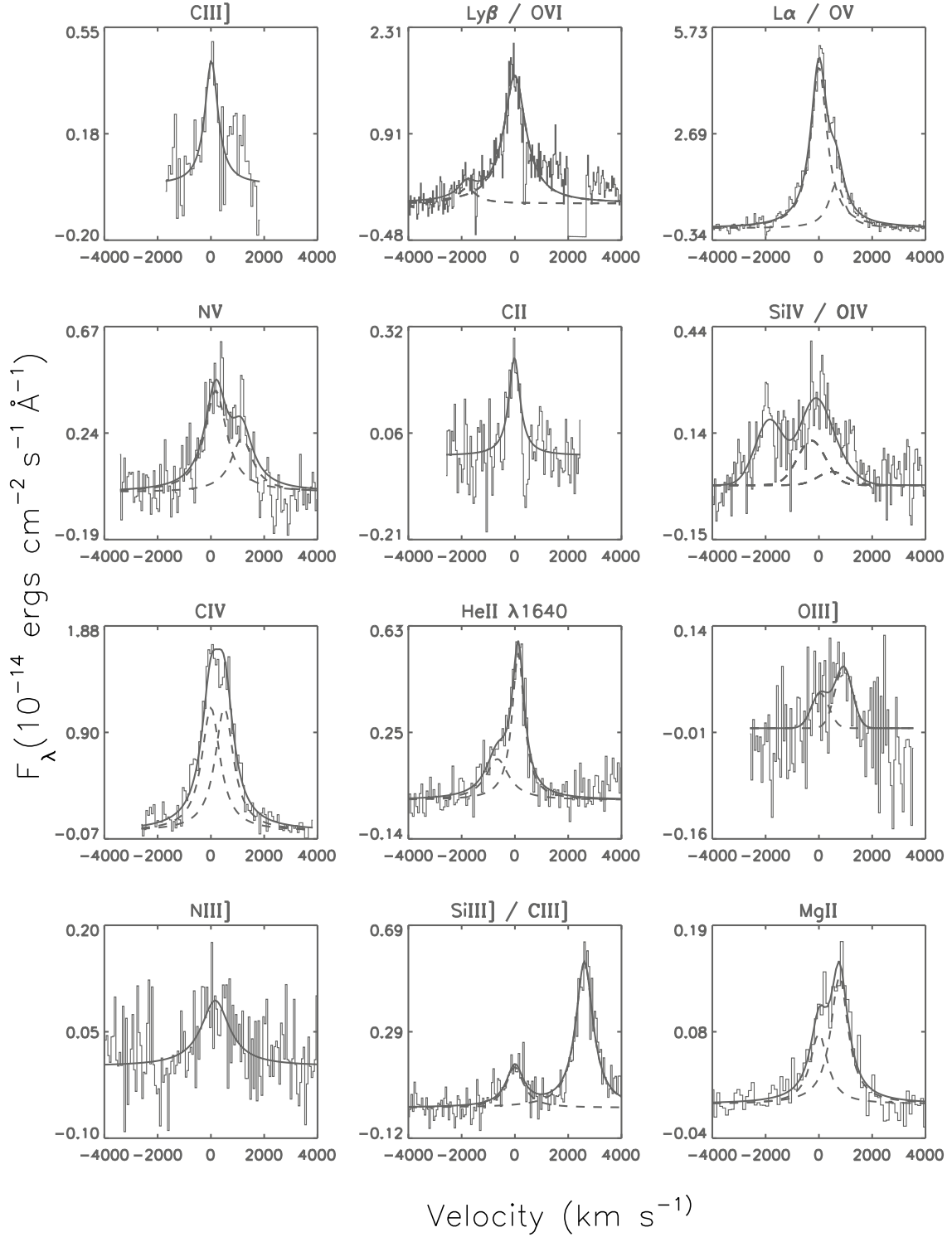


Fig. 3.— The models for the emission lines in the RE 1034+39 spectra, after continuum subtraction. All emission lines are consistent with a Lorentzian profile.

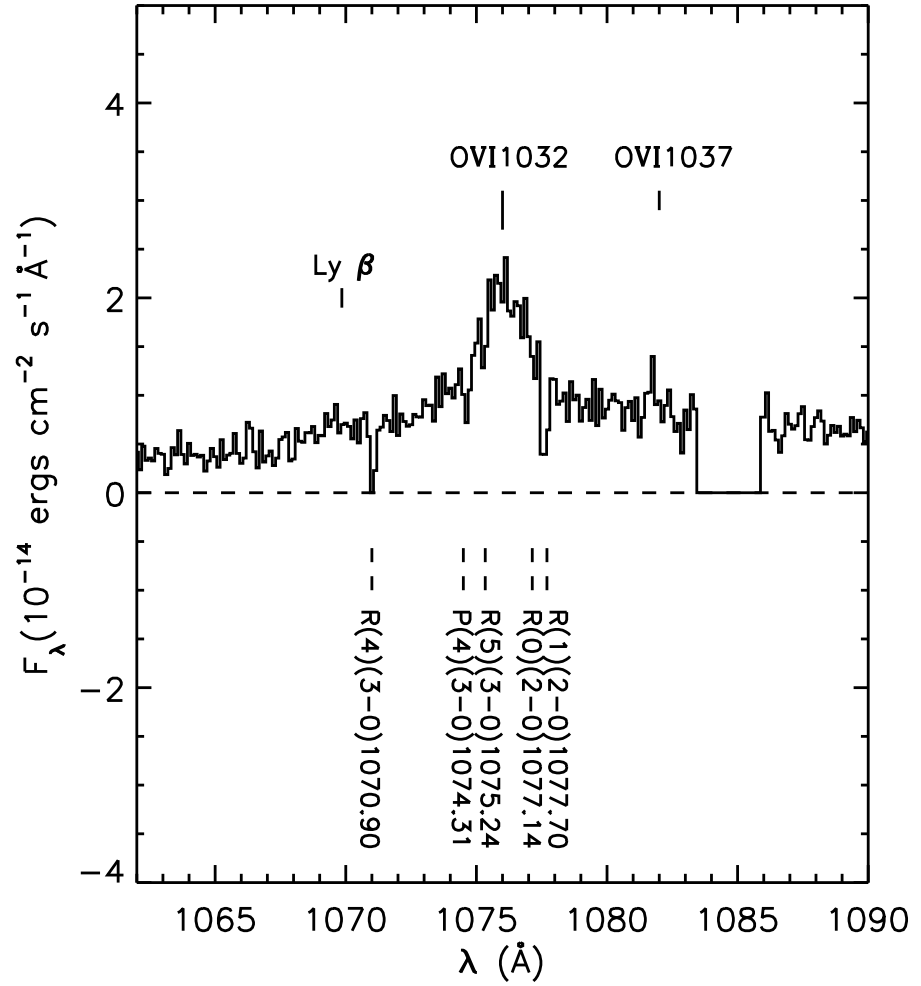


Fig. 4.— The region of the spectrum containing O VI and Ly β . The rest-frame positions of the emission lines are labeled above the plot; the Galactic absorption lines are labeled below. All absorption lines are consistent with zero redshift molecular hydrogen transitions originating in our Galaxy; no absorption lines intrinsic to the AGN are observed.

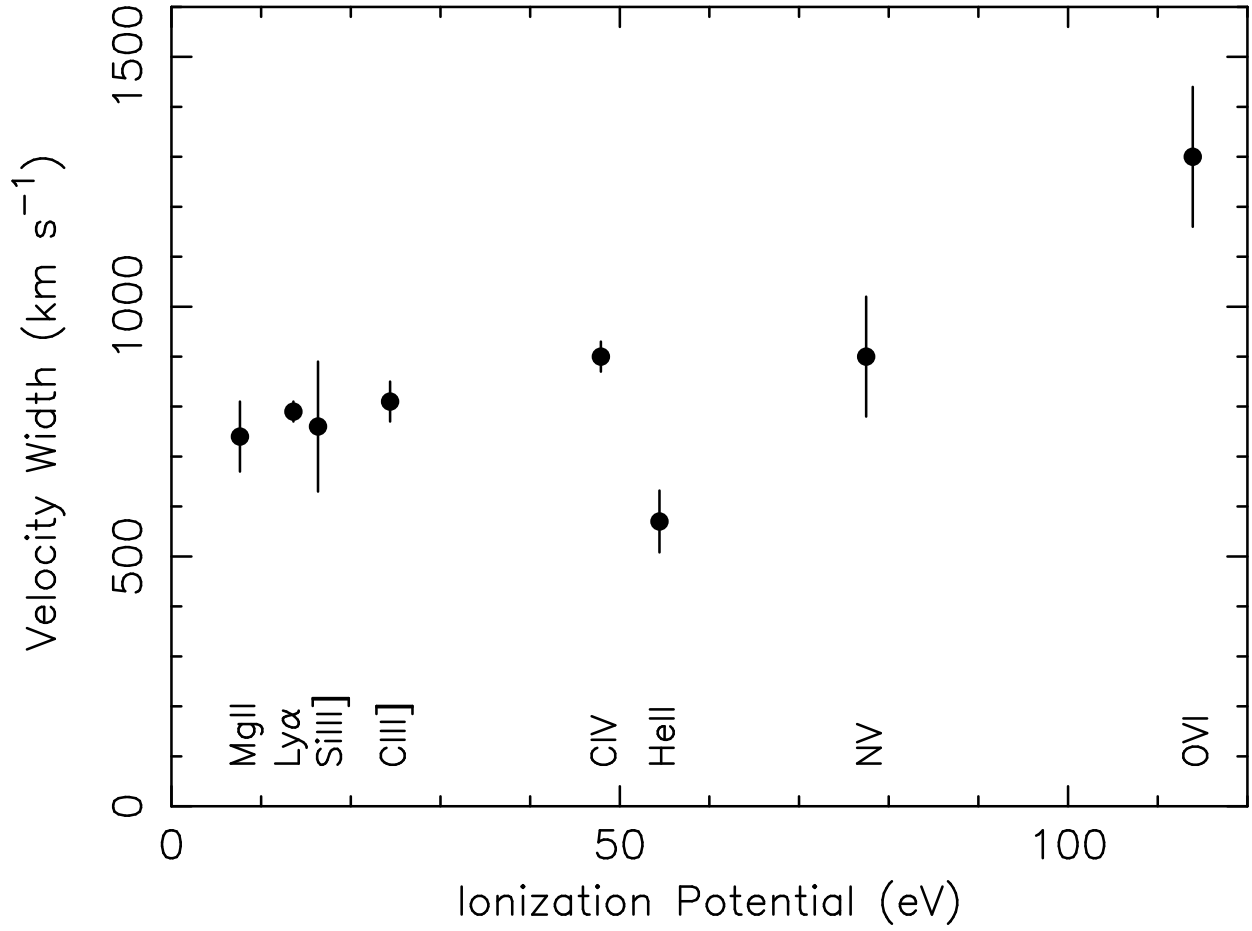


Fig. 5.— The velocity width (FWHM) as a function of ionization potential for the brighter and least-blended FUV and UV emission lines. A slight increase in velocity width potentially indicates stratification of the emission line region. The exception is He II which differs from the other lines because it has a blue wing; deblending the blue wing may result in a narrower core.

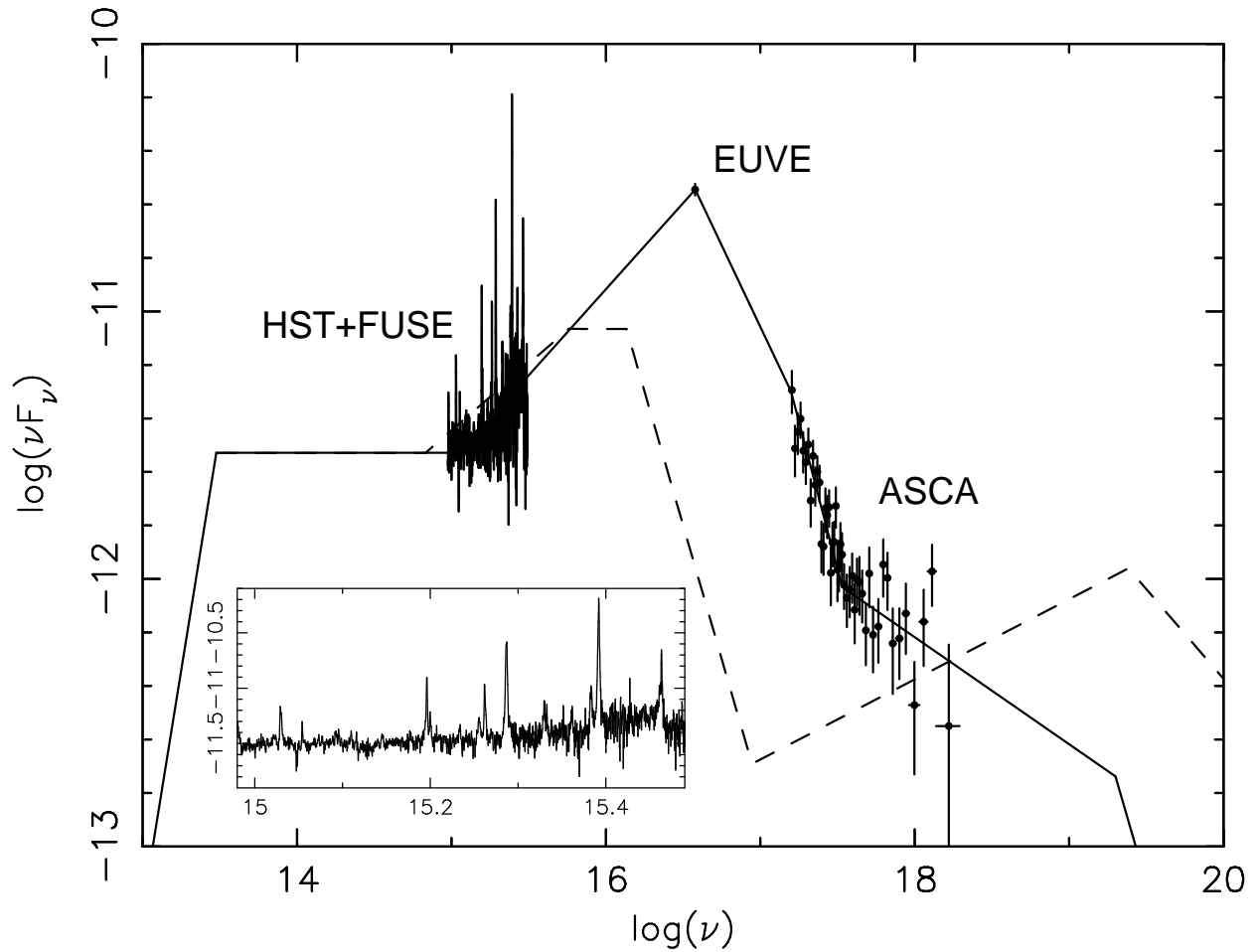


Fig. 6.— The adopted continuum for *Cloudy* simulations was constructed from the simultaneous *FUSE*, *EUVE* and *ASCA* data, and the nonsimultaneous *HST* data. The *Cloudy* AGN continuum is shown for comparison (dashed line). The inset shows the subtle upturn in the UV continuum toward high frequencies.

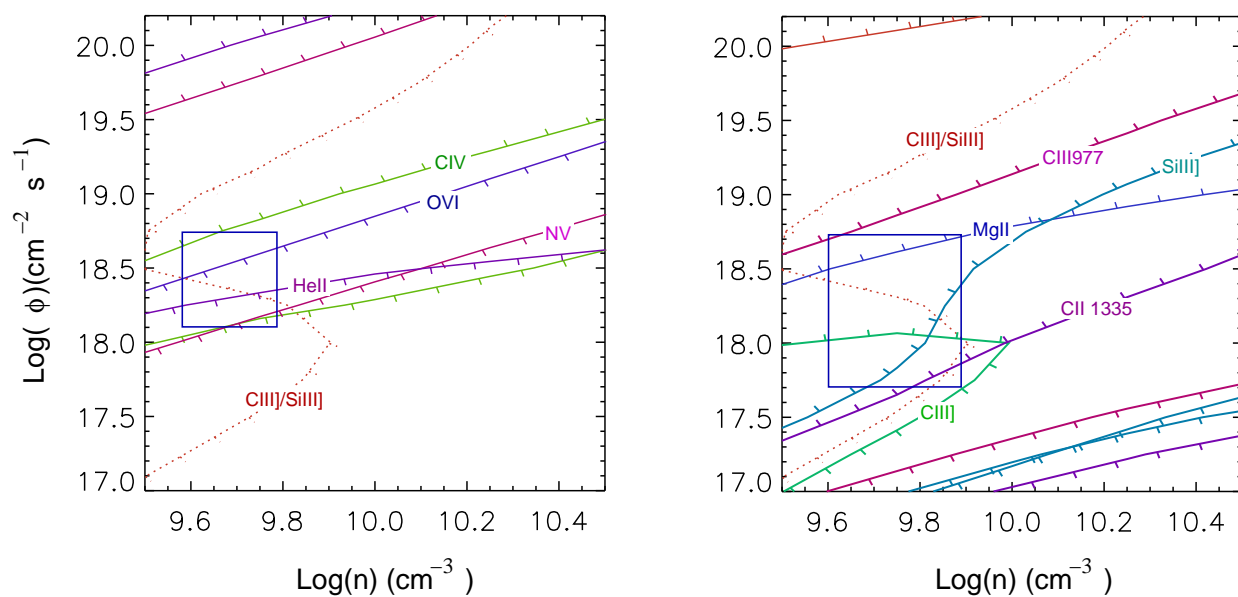


Fig. 7.— Cloudy model results for the high-ionization lines (left) and the intermediate- and low-ionization lines (right). The dotted line shows the ratio of C III] to Si III], a parameter that should be sensitive to density. The contour ticks mark the direction of decreasing equivalent width. The boxes delineate the region of parameter space that is intersected by all contours.

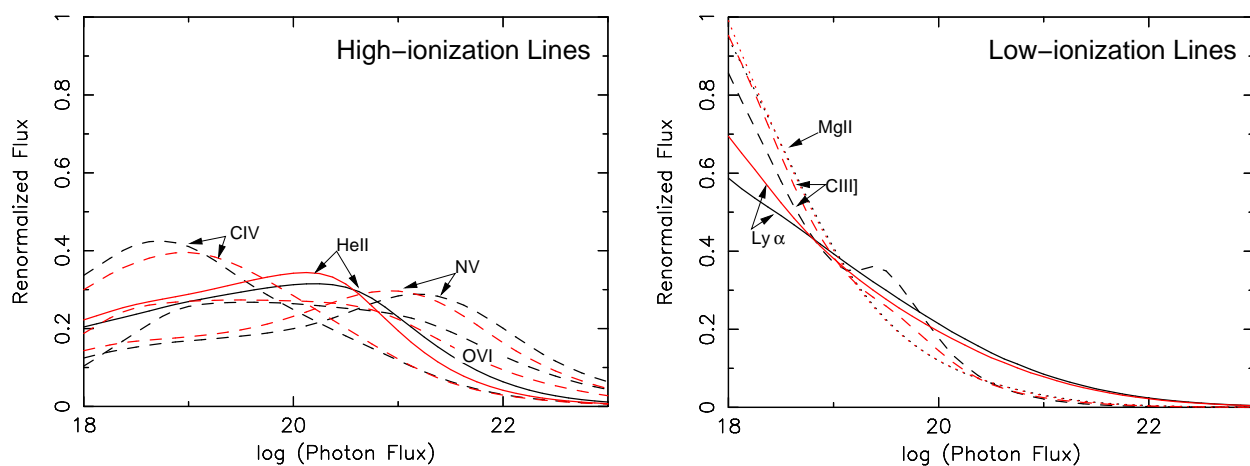


Fig. 8.— Renormalized line emissivity for a 2-d, flattened geometry for LOC models. The left plot shows the results for the high-ionization lines, and the right plot shows the results for the intermediate- and low-ionization lines. The red and black lines show the results for the RE 1034+39 and AGN continua, respectively. Little difference is seen between these two continua; however, the emission is distributed over a much larger $\Delta\Phi$ than is implied by the difference in the velocity widths of the lines. The emissivity of the low-ionization lines rises strongly toward large radii (low fluxes) perhaps indicating sensitivity of these lines to the value of the lowest Φ used in LOC models.

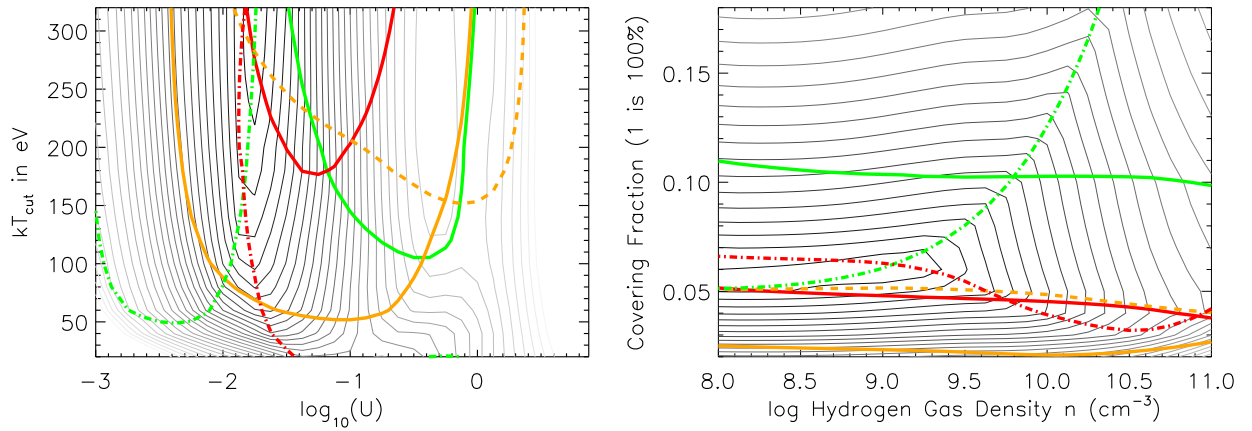


Fig. 9.— Cloudy model results for cuts through the FOM matrix around the global minimum located at $kT_{cut} = 240$ eV, $\log(U) = -1.8$, $\log(n_H) = 9.125$, and covering fraction of 6%. The spectral energy distribution parameterized by kT_{cut} versus the ionization parameter $\log(U)$ (*left*) and the covering fraction versus the hydrogen density $\log(n_H)$ (*right*) are shown. The thin, grayscale contours show the FOM with interval of 0.4, and with the darker contours in the minimum. The thick colored contours show where the model line fluxes equal the measured line fluxes with the following key: green – O VI; red – N V; orange – C IV; dashed orange – He II; dash-dot red – Si III; dash-dot green – C III] (i.e., permitted lines are solid, recombination lines are dashed, and intercombination lines are dash-dotted.)

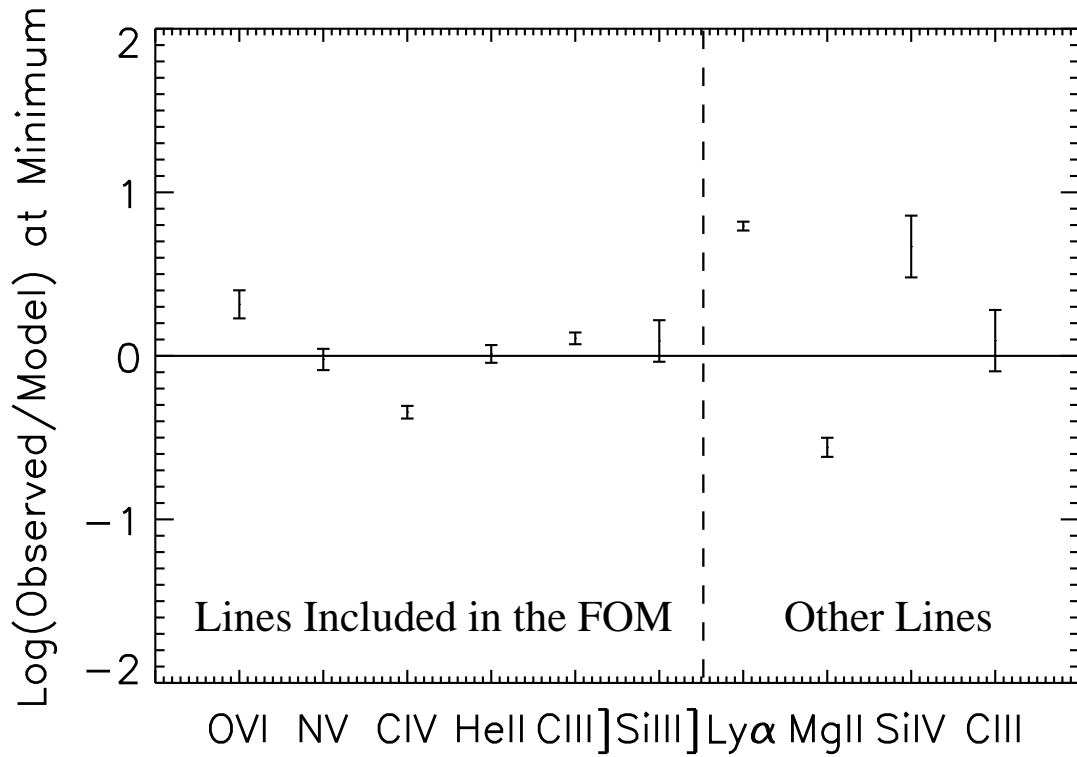


Fig. 10.— The log of the ratio of the observed line fluxes with model line fluxes. Error bars indicate statistical uncertainty from the spectral fitting. The six lines on the left were used to construct the *FOM*.

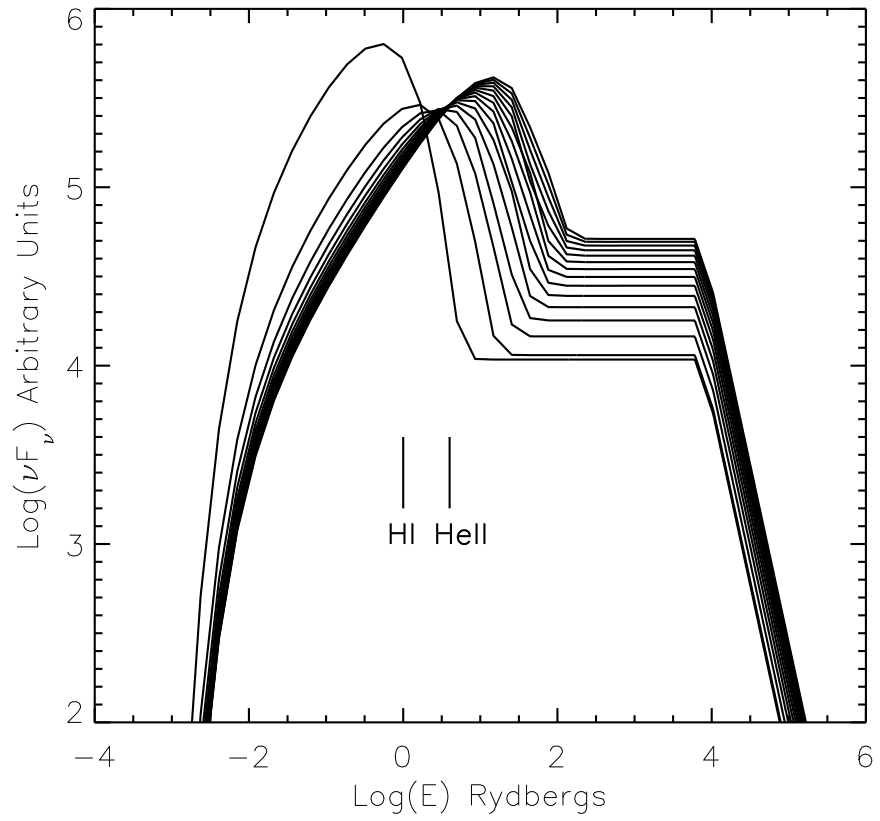


Fig. 11.— A representative set of the semi-empirical spectral energy distributions used in §7, normalized so that they all yield the same value of the ionizing flux.

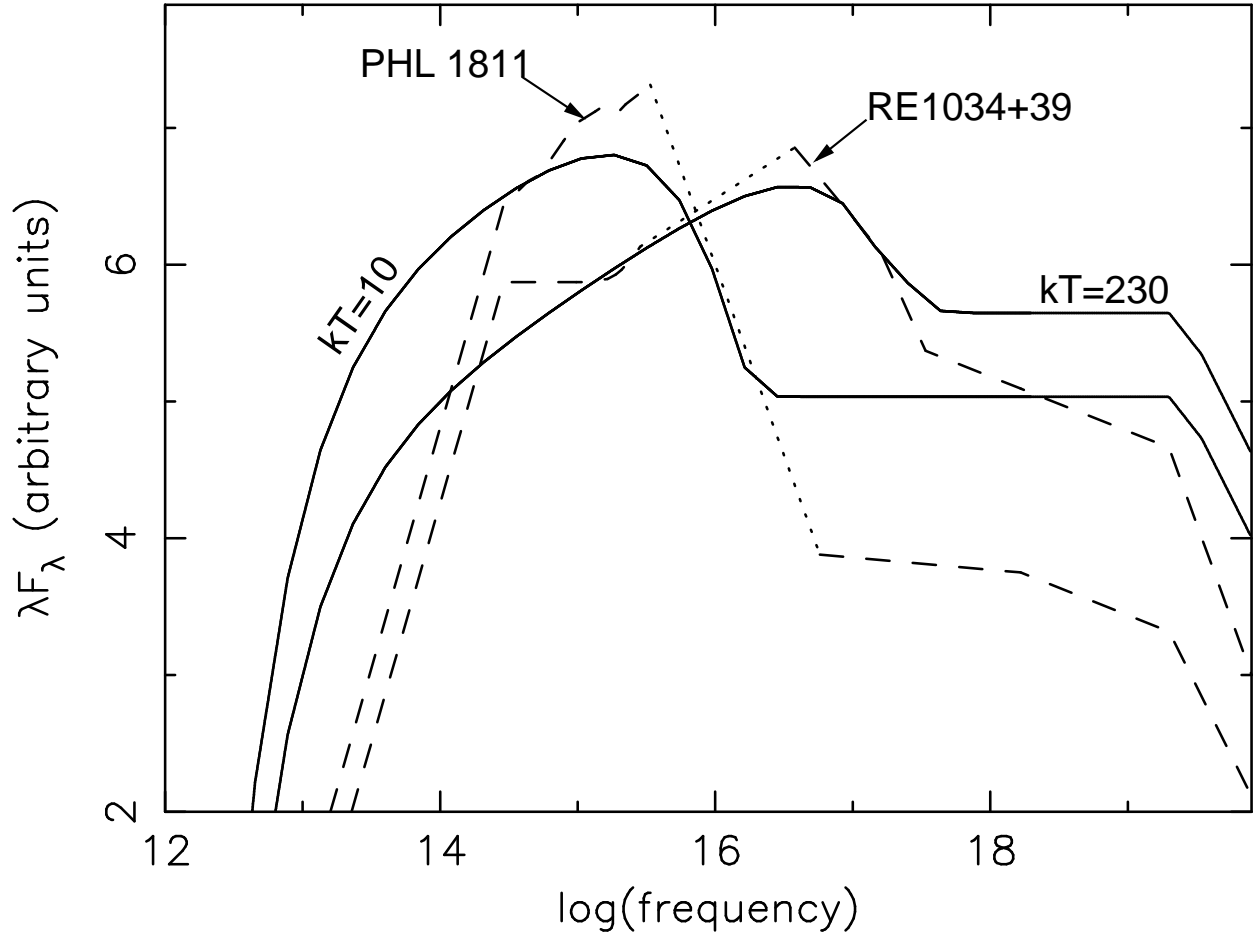


Fig. 12.— Comparison of observed SEDs (solid lines) from coordinated observations with the semi-empirical spectral energy distributions (dashed lines; dotted lines in the unobservable EUV), illustrating that the semi-empirical SEDs correspond fairly well with observed ones.

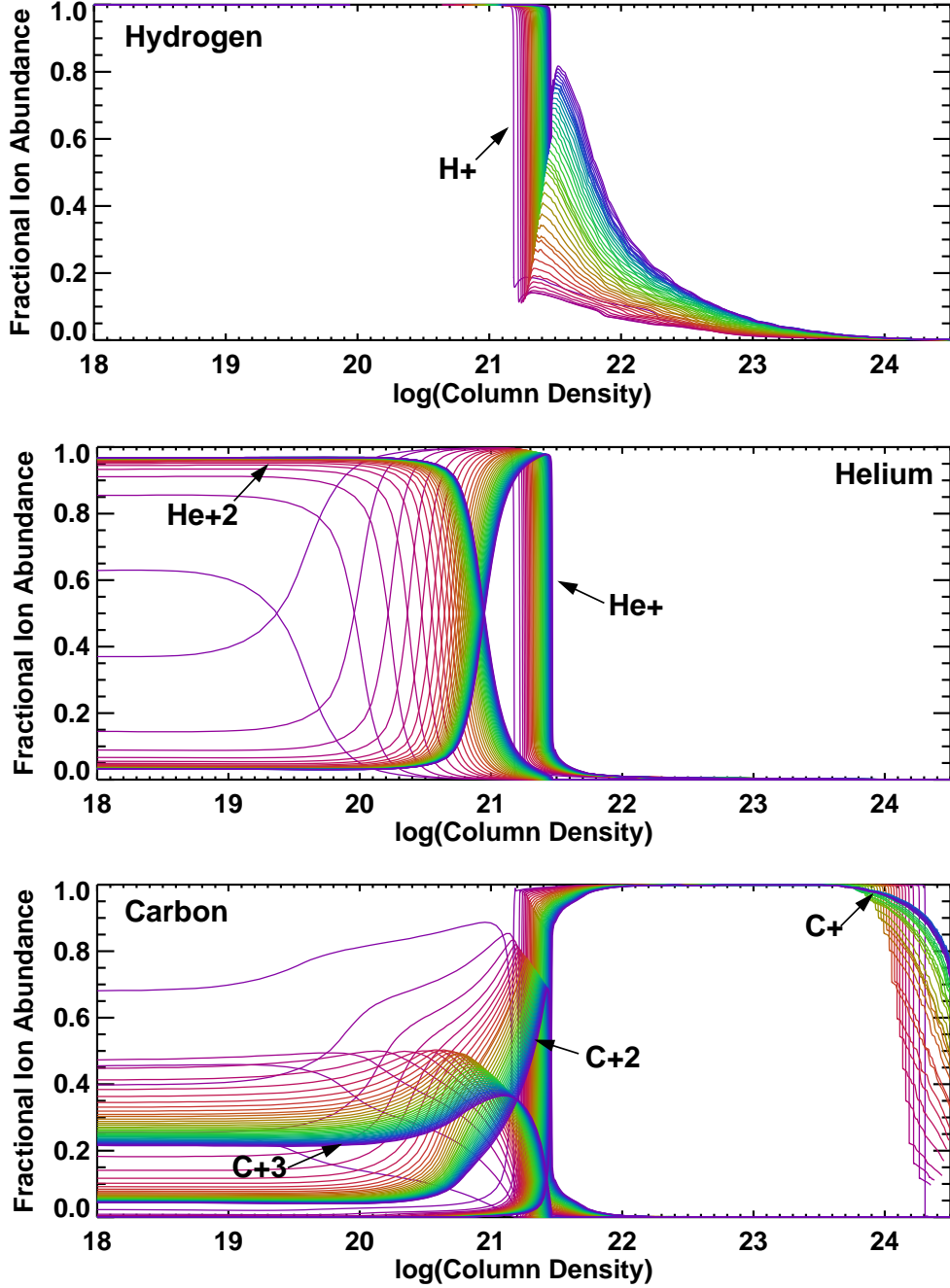


Fig. 13.— The ionization fraction for select ions of hydrogen, helium and carbon as a function of column density for the semi-empirical SEDs. We assume $\log U = -2$, $\log n_H = 10$, and $\log N_H = 26$ for illustration. Red lines corresponds to lower values of kT (soft continua), and blue corresponds to higher values of kT (harder continua). Notable differences include a deeper partially-ionized zone for hydrogen H^+ for the harder continua, deeper He I region but shallower He II region for the softer continua, and overall low ionization at small column density for softer continua.

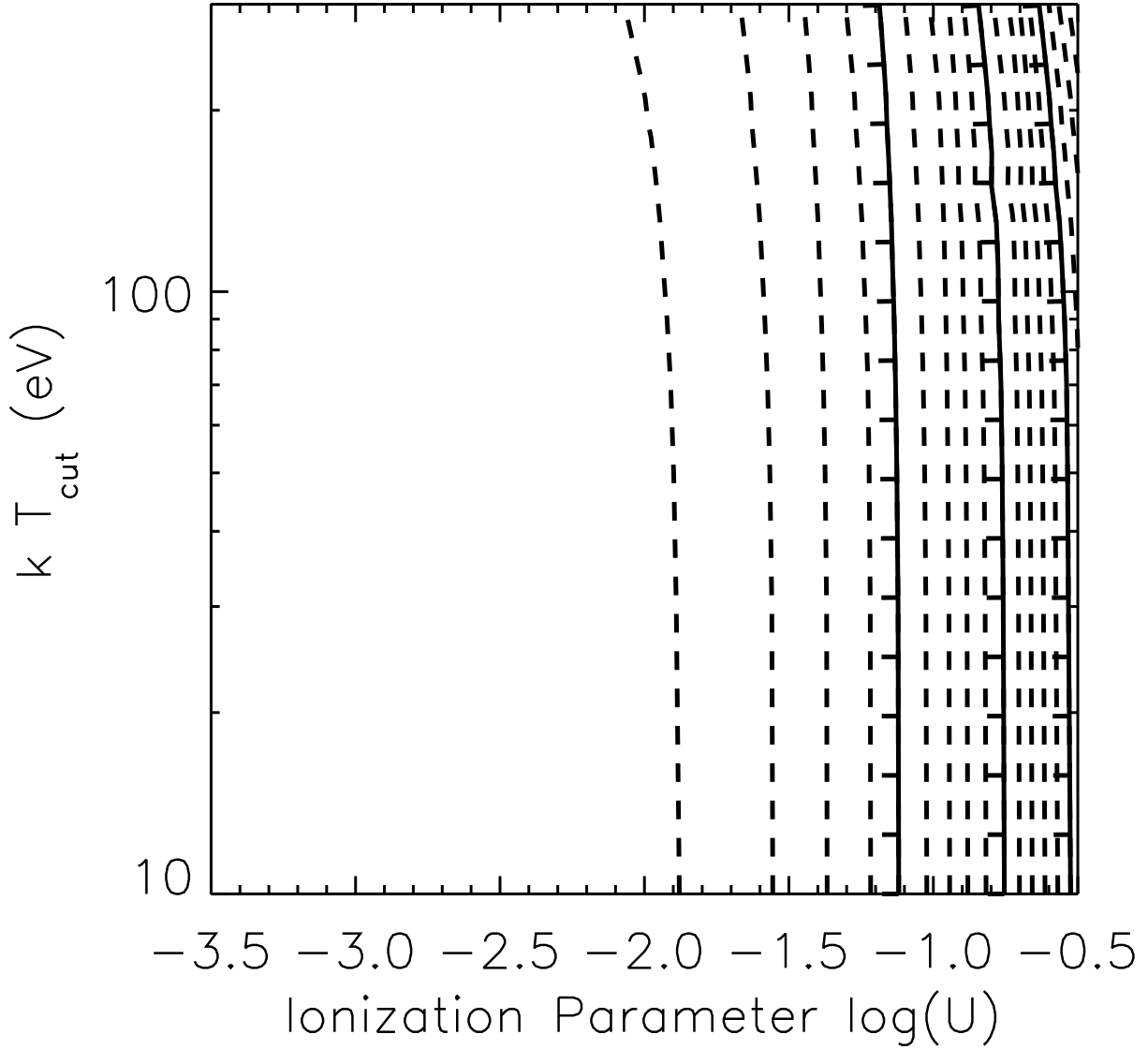


Fig. 14.— The contours of Ly α flux as a function of $\log(U)$ and kT . This shows that Ly α flux is almost independent of spectral energy distribution, as expected. By dividing other line flux values by the Ly α , we can partially remove the ionization parameter dependence.

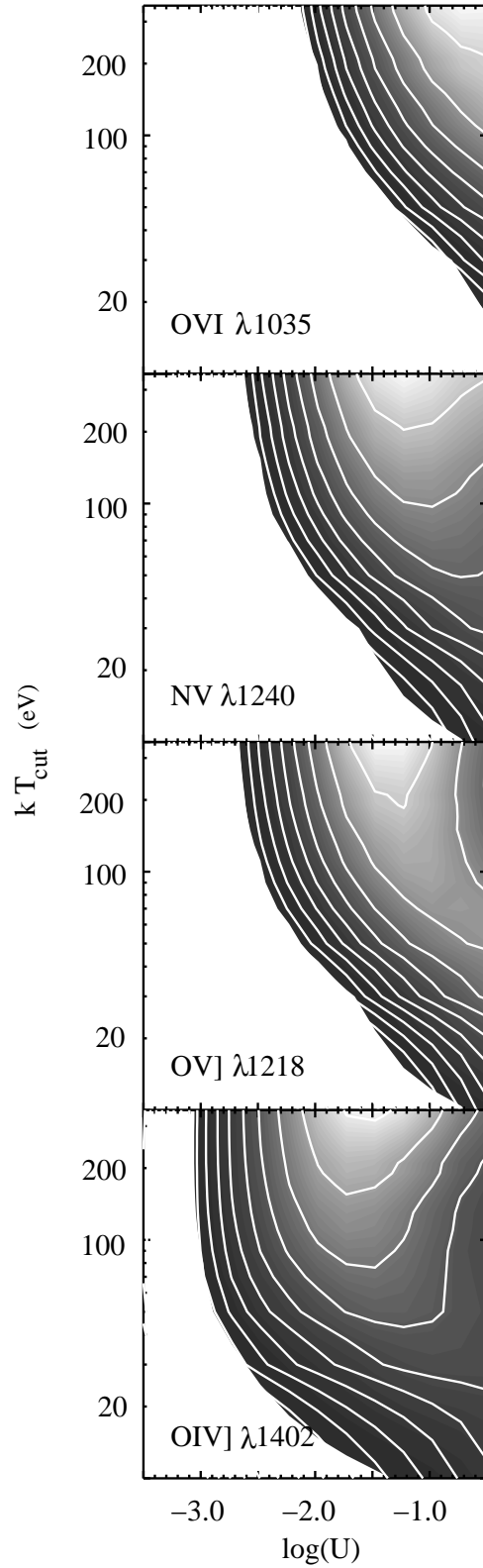


Fig. 15.— Ratios of lines from ions with I.P. > 54.4 eV with Ly α . Shading shows the whole range for each emission line; contours increase by a factor of 1.25. The density for these simulations is $n_H = 10^{10} \text{cm}^{-3}$.

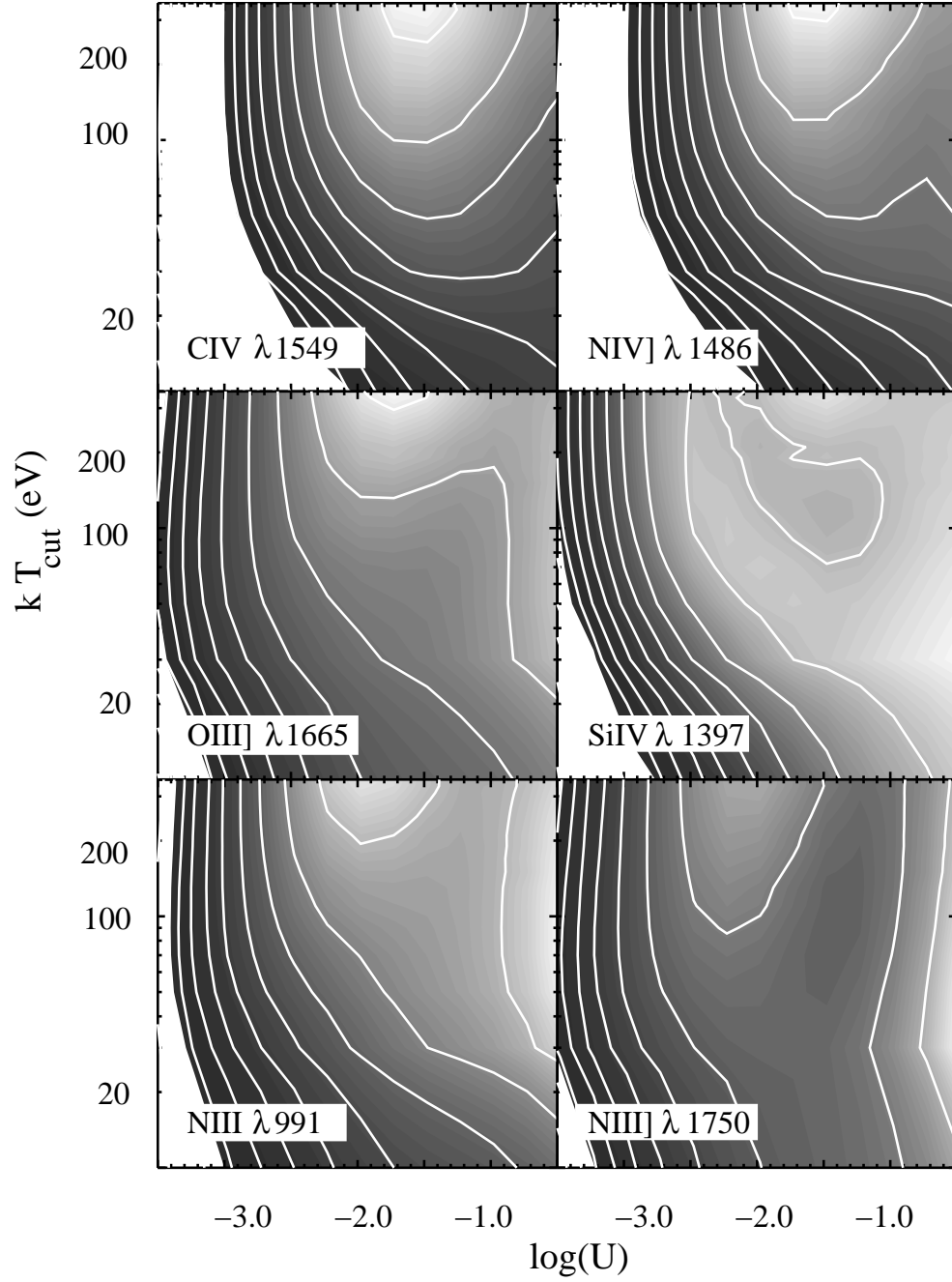


Fig. 16a.— Ratios of lines from ions with $13.6 < \text{I.P.} < 54.4 \text{ eV}$ with $\text{Ly}\alpha$.

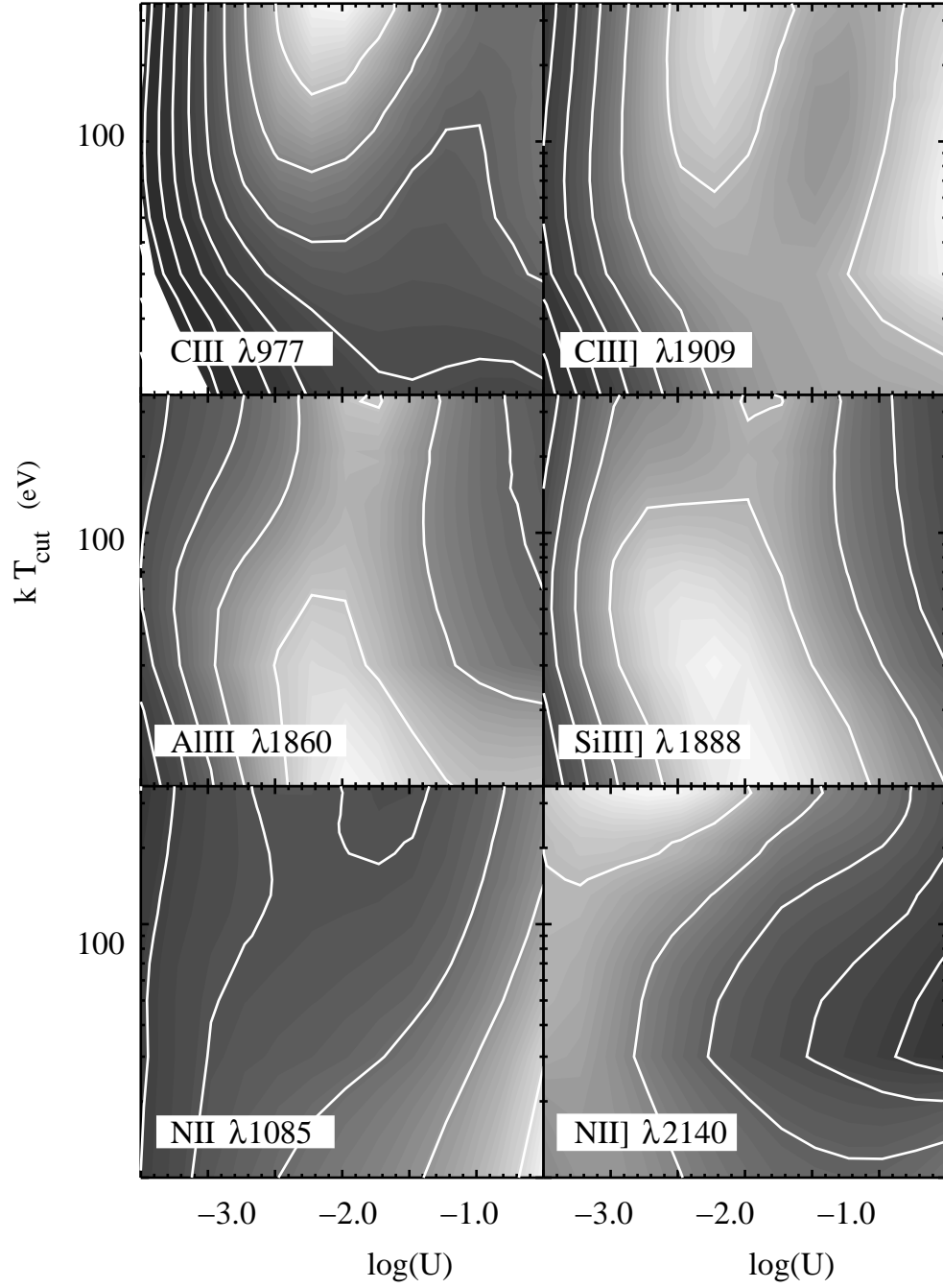


Fig. 16b.— Fig. 16 continued.

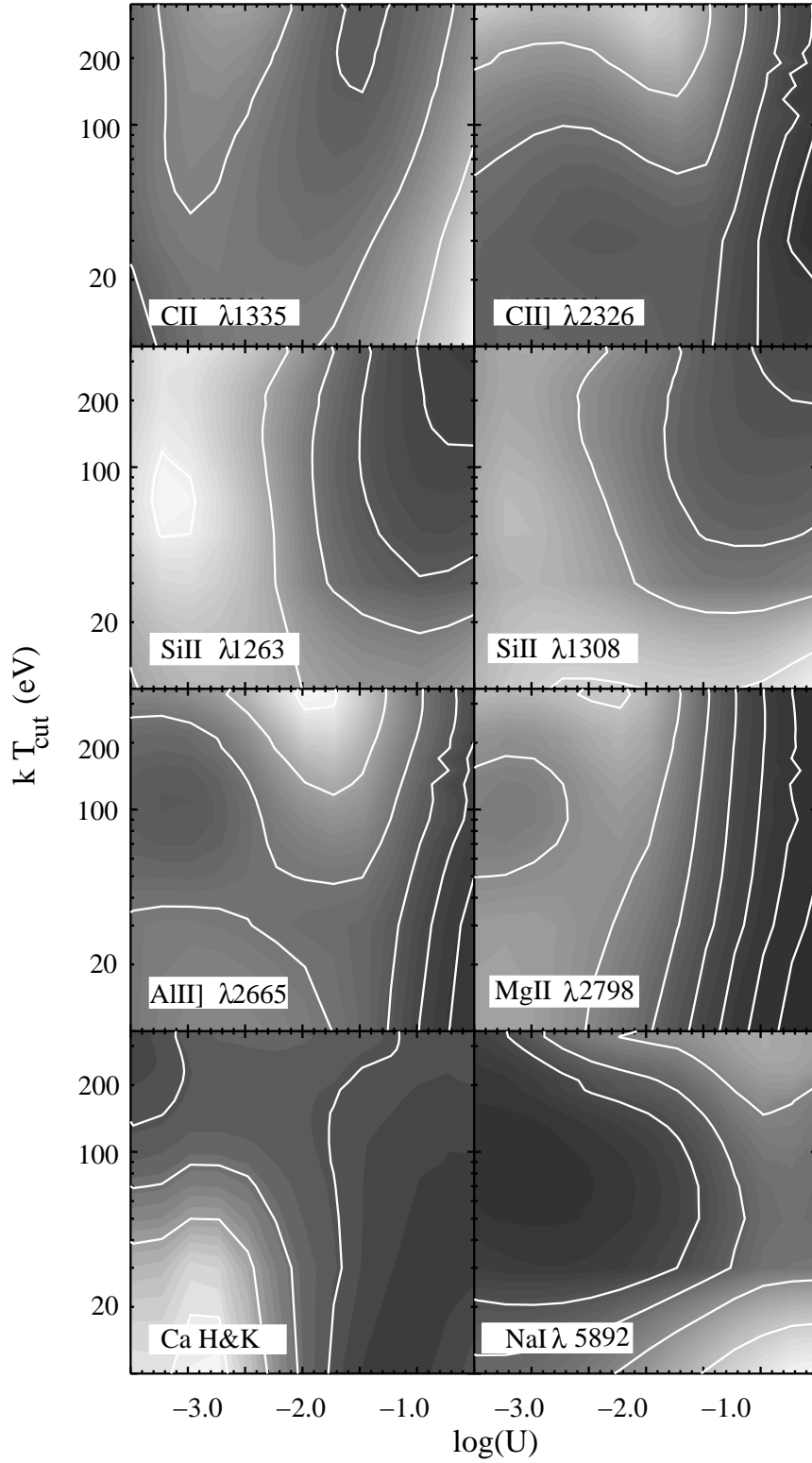


Fig. 17.— Ratio of lines from ions with I.P. < 13.6 eV with $\text{Ly}\alpha$.

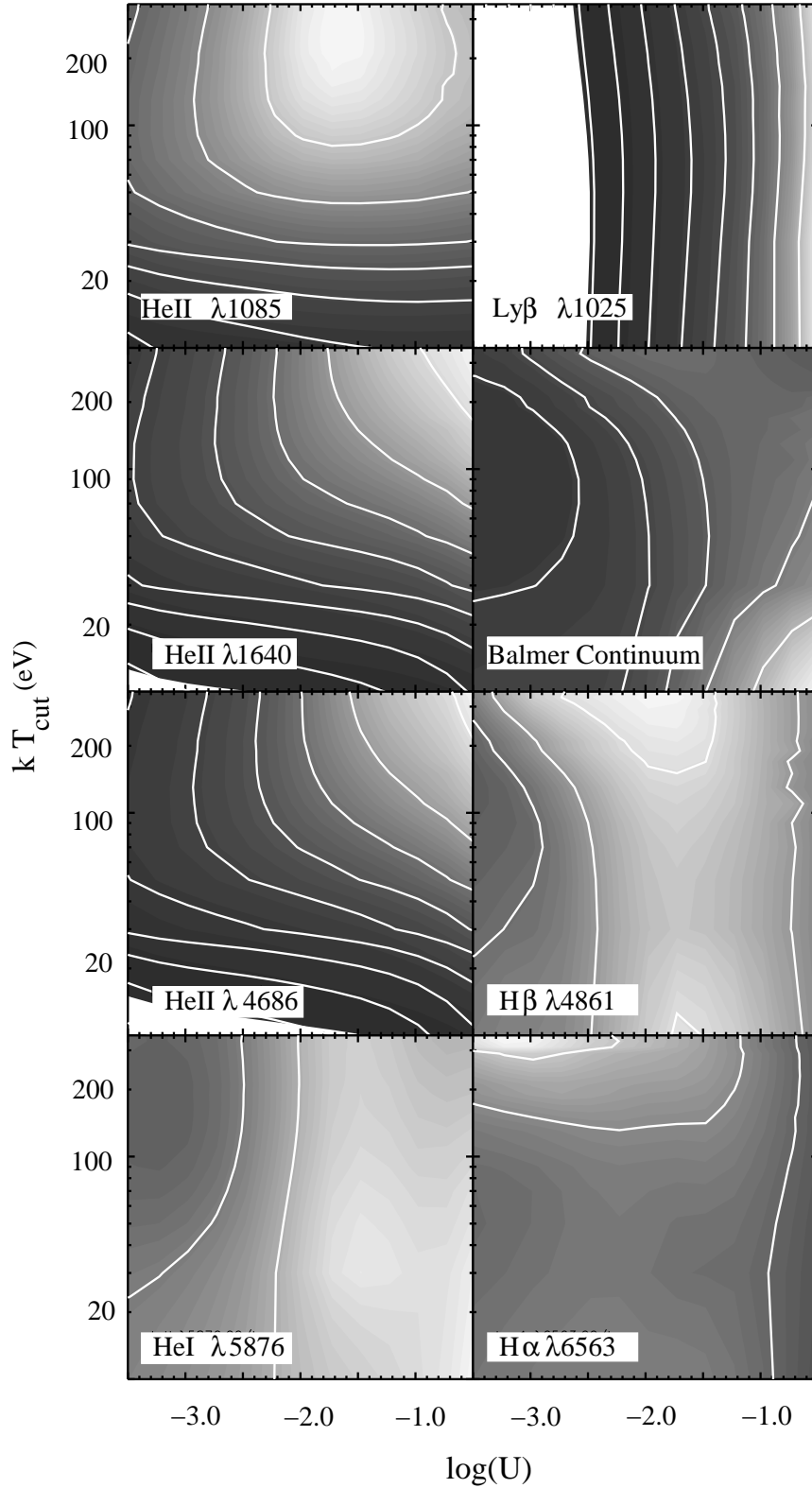


Fig. 18.— Ratio of recombination lines with Ly α .

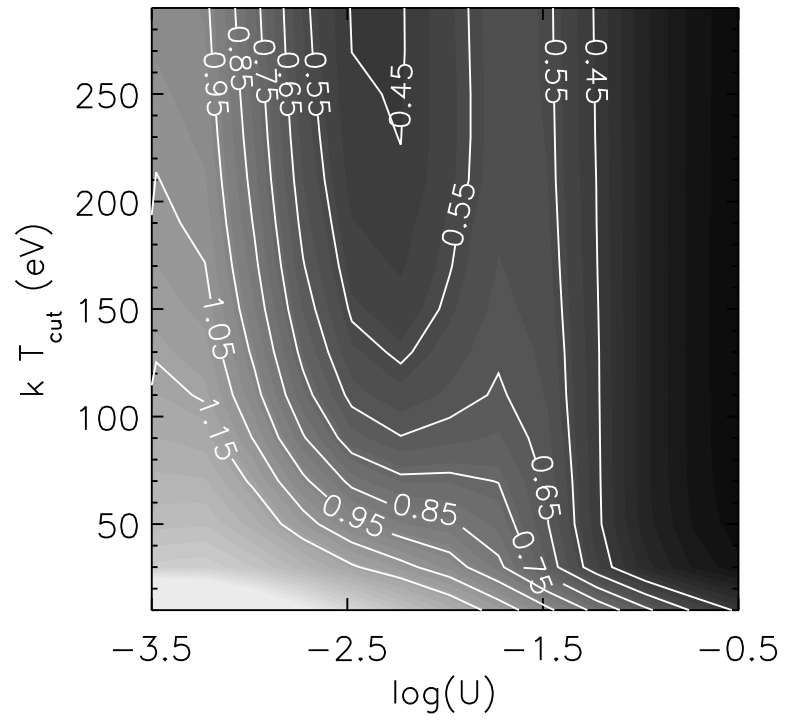


Fig. 19.— Contours for the density indicator $\text{Si III]}/\text{C III]}$. Significant variations in the kT_{cut} direction indicate that $\text{Si III]}/\text{C III]}$ is not independent of the spectral energy distribution.

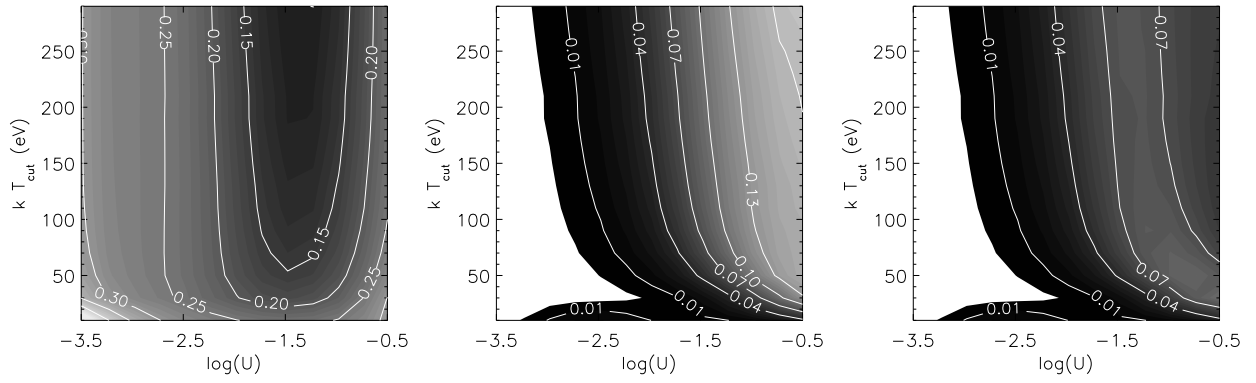


Fig. 20.— Contours for the metallicity indicators. Left: $N\ III]/O\ III]$; middle: $N\ V/C\ IV$; right: $N\ V/(O\ VI+C\ IV)$. Variations in the kT_{cut} direction reveal that the metallicity indicators are not robust for the softest spectral energy distributions.

Table 1. Observing Log

Observatory	Date	Bandpass	Exposure (seconds)
<i>FUSE</i>	2000 April 30 20:50:43 – 2000 May 3 02:32:18	905–1187 Å	43,640
<i>ASCA</i>	2000 May 1 00:14–12:37	0.6–10 keV (SIS)	15,700
		0.8–10 keV (GIS)	17,500
<i>EUVE</i>	2000 April 1:27:59 – 2000 May 2 20:57:59	0.15 keV	63,700
<i>HST</i> FOS	1997 January 31	G130H (1140–1605)	4,420
		G190H (1575–2330)	2,460
		G270H (2220–3300)	670

Table 2. Spectral parameters in the X-ray band

Correction ^a	Photon index (Γ)	PL Norm. ^b	$kT(\text{keV})$ ^c	BB Norm. ^d	$\chi^2_{\nu}/\text{d.o.f}$
Without	$2.28^{+0.18}_{-0.20}$	$6.4^{+1.3}_{-1.2}$	0.152 ± 0.017	1.3 ± 0.3	1.13/149
With	$2.35^{+0.17}_{-0.16}$	$7.1^{+1.1}_{-1.1}$	0.122 ± 0.014	3.4 ± 0.9	1.13/138

^aCorrection for SIS data included or not.

^bThe power-law normalization in units of 10^{-4} photons $\text{cm}^{-2} \text{s}^{-1} \text{keV}^{-1}$ at 1 keV in the source rest frame.

^cThe blackbody temperature in the source rest frame.

^dSource luminosity in units of 10^{34} ergs s^{-1} assuming it is located at 10 kpc. The luminosity distance is 190.2 Mpc using cosmological parameters of $H_0 = 70 \text{ km s}^{-1} \text{Mpc}^{-1}$, $\Lambda_0 = 0.70$, and $\Omega_M = 0.3$.

Table 3. Prominent Emission Line Measurements

Emission Line	measured $\lambda(\text{\AA})^{a,b,c}$	Laboratory $\lambda(\text{\AA})^a$	FWHM (km s^{-1}) ^d	$F(10^{-14} \text{ ergs s}^{-1} \text{ cm}^{-2})^c$	$W_\lambda(\text{\AA})$
C III	977.4 ± 0.2	977.0	1170 ± 540	1.6 ± 0.3	4.1
Ly β	1028.3 ± 1.2	1025.7	1220 ± 620	0.20 ± 0.12	0.5
O VI	1031.7 ± 0.06	1031.9	1300 ± 140	11.2 ± 1.0	28.8
Ly α	1215.9 ± 0.02	1215.7	790 ± 20	22.2 ± 0.6	49
O V]	1218.3 ± 0.2	1218.3	1020 ± 130	6.5 ± 0.8	14.4
N V	1239.4 ± 0.2	1238.8	900 ± 120	2.6 ± 0.3	5.8
	1243.4 ± 0.2	1242.8	900 ± 120	1.4 ± 0.2	3.1
C II	1334.4 ± 0.3	1334.5	300 ± 90	0.7 ± 0.5	1.6
O IV]	1399.7		1120 ± 70	0.09 ± 0.06	0.23
	1401.2		1120 ± 70	0.51 ± 0.06	1.3
	1404.8		1120 ± 70	0.14 ± 0.06	0.31
	1407.3		1120 ± 70	0.09 ± 0.06	0.20
Si IV	1393.8 ± 0.3	1393.8	1120 ± 70	1.33 ± 0.22	3.0
	1402.8 ± 0.3	1402.8	1120 ± 70	1.37 ± 0.47	3.0
C IV	1548.0 ± 0.08	1548.2	900 ± 30	7.9 ± 0.4	14.4
	1550.5 ± 0.08	1550.8	900 ± 30	8.4 ± 0.5	15.2
He II (blueshifted)	1637 ± 0.1^e	1640.4	700 ± 140	1.0 ± 0.2	1.8
He II	1640.7 ± 0.1	1640.4	570 ± 60	2.7 ± 0.3	5.0
O III]	1661.0 ± 1.4	1660.8	810 ± 40	0.45 ± 0.21	0.8
	1666.3 ± 0.7	1666.2	810 ± 40	1.0 ± 0.18	1.8
N III]	1751.0 ± 0.5	1750.4	810 ± 40	0.62 ± 0.13	1.1
Si III]	1892.3 ± 0.3	1892.0	760 ± 130	1.18 ± 0.15	2.1
C III]	1909.1 ± 0.08	1908.7	810 ± 40	4.45 ± 0.16	8.1
Mg II	2796.4 ± 0.3	2796.4	740 ± 70	1.0 ± 0.09	5.0
	2803.6 ± 0.3	2803.5	740 ± 70	1.4 ± 0.10	7.0

^aVacuum wavelengths for $\lambda < 3000\text{\AA}$; Air wavelengths for $\lambda > 3000\text{\AA}$.

^bNo entry in this column means that the wavelengths were fixed at the laboratory wavelength for the purpose of deblending weak lines.

^cRepeated uncertainties in these column mean that the flux ratios were constrained in the fitting.

^dRepeated values in this column mean that the widths were constrained to be equal in the fitting.

^eA blueshifted component was observed on He II; this is the central wavelength of that component.

Table 4. Emission Line Comparison

Emission line ^a	RE 1034+39 Relative Flux	Relative Flux		
		Francis	Zheng ^a	Brotherton
Ly β +O VI	102 ^c	9.3	16.0	11.6
Ly α +N V feature	118	100		100
Ly α	100		100	
N V	18.0		14.0	
1400 Å feature	15.9	19	8.1	6.8
He II	16.8 ^b	18 ^d	3.4	5.2 ^d
C IV	73	63	52	27
1900 Å feature	25.4	29		10
Al III	0.0		2.9	
Si III]	5.3		2.8	
C III]	20.0		12	
Mg II	10.8	34	33	13

^aRadio-quiet quasars.

^bSum of blueshifted and rest frame components..

^cAssuming that the 1037Å and 1031Å lines have the same flux (optically thick). The value would be 77 if the lines have 2:1 ratio (optically thin).

^dHe II λ 1640+O III] λ 1666.

Table 5. LOC model results

Emission Line	Baldwin ^{a,b}	Baldwin Re-created ^{a,c}	RE 1034+39 SED ^a	RE 1034+39 (measured) ^a
O VI λ 1032 + Ly β	0.16	0.19	0.52	0.51
Ly α	1.0	1.0	1.0	1.0
N V	0.04	0.067	0.18	0.18
O IV]+Si IV	0.06	0.05	0.17	0.16
C IV	0.57	0.54	1.11	0.73
O III] + He II λ 1640	0.14	0.16	0.25	0.11 ^d
Mg II	0.34	0.29	0.47	0.11

^aFlux ratios with respect to Ly α .

^bThe results taken from Balwin et al. 1995.

^cOur re-creation of the Balwin et al. (1995) results.

^dOnly narrow, restframe component of He II is included.